

2.02 Fuel Performance of Light Water Reactors (Uranium Oxide and MOX)[☆]

Daniel Baron, Electricity of France, Moret-sur-Loing, France

Lars Hallstadius, Westinghouse Electric Sweden AB, Västerås, Sweden

Katalin Kulacsy, Centre for Energy Research, Budapest, Hungary

Rodrigue Largenton, Electricity of France, Moret-sur-Loing, France

Jean Noirot, CEA, DES, IRESNE, DEC, Cadarache F-13108, Saint-Paul-Lez-Durance, France

© 2020 Elsevier Ltd. All rights reserved.

2.02.1	Introduction	36
2.02.2	Experience of Oxide Fuel in LWRs	37
2.02.2.1	History of Development	37
2.02.2.2	Fuel Elements Design	39
2.02.2.2.1	The fuel pellets	39
2.02.2.2.2	The fuel rod cladding	41
2.02.2.2.3	Use of additives in the fuel	41
2.02.2.2.4	The fuel rod assemblies	41
2.02.2.3	LWR Operating Conditions	42
2.02.2.3.1	PWR normal operating conditions	42
2.02.2.3.2	BWR normal operating conditions	44
2.02.3	Behavior at Beginning of Life	45
2.02.3.1	Basic Irradiation Effects	45
2.02.3.2	Thermal Aspects	46
2.02.3.3	Mechanical Aspects	49
2.02.3.4	Material Microstructure and Chemistry	52
2.02.4	Consequences of Burnup Accumulation	53
2.02.4.1	Burnup	53
2.02.4.2	Behavior of the Gaseous and Volatile Fission Products	54
2.02.4.3	Evolution of the Oxygen Potential	59
2.02.4.4	Evolution of the Properties	59
2.02.4.5	Grain Restructuring	60
2.02.4.5.1	HBS grain restructuring at the UO ₂ fuel periphery and in MOX Pu-rich zones	60
2.02.4.5.2	UO ₂ fuel central area grain restructuring	63
2.02.5	Transient Conditions	64
2.02.6	Limiting Phenomena	67
2.02.7	Conclusions	68
References		68

Abbreviations

ASTM American Society for Testing and Material (international standards organization)
BWR boiling water reactor
CEA Commissariat à l'Energie Atomique et aux Energies Alternatives (France)
EDF Electricité De France
EPMA electron probe micro analysis
FBR fast breeder reactors
GCR gas cooled reactors
HBEP high burnup effect program
HBRP high burnup rim project

HBS high-burnup structure
IAEA International Atomic Energy Agency
LWR light water reactor
MIMAS micronisation master blend
MOX mixed-oxides fuel
NFIR nuclear fuel industry research group
NXO new cross-over project
PCI pellet-cladding interaction
PCMI pellet-cladding mechanical interaction
PHWR pressurized heavy water reactor
PWR pressurized water reactor
RIA reactivity insertion accident

[☆]Change History: September 2019. Daniel Baron, Lars Hallstadius, Katalin Kulacsy, Rodrigue Largenton and Jean Noirot have updated the figures text and references. This is an update of Baron, D.D., Hallstadius, L., 2012. Chapter 2.19 – Fuel Performance of Light Water Reactors (Uranium Oxide and MOX). In: Konings, R.J.M. (Ed.), Comprehensive Nuclear Materials, Elsevier, pp. 481–514.

RMBK russia high power channel-type reactor
 SCC stress corrosion cracking
 SEM scattering electron microscopy

TEM transmission electron microscopy
 XRD X-ray diffraction

2.02.1 Introduction

Historically, mainly because of their very simplified and safe design, pressurized water reactors (PWRs) and boiling water reactors (BWRs) are representing the two designs most commonly used for electricity production for the last 60 years. In 2019, 449 reactor units were operated worldwide, out of which 299 were PWR, and 71 were BWR. Altogether, 390 (82% of all reactor units) were therefore light water reactor (LWR) units ([Fig. 1](#)).

These LWR units are mainly loaded with uranium dioxide (UO_2) with an average enrichment ranging between 3.5% and 5% in isotope 235 (natural uranium contains only 0.72% of this isotope). However, Europe and Japan have practiced the recycling of plutonium for more than 30 years, introduced in mixed oxides (MOX, $(\text{U},\text{Pu})\text{O}_2$), mostly manufactured by a two-stage powder mixing process. In the LWR designs, purified light water with controlled pH plays the roles of both moderator and coolant, flowing up from the bottom to the top of the core. The BWR design allows the water to achieve bulk boiling, starting near the bottom of the core, with a primary circuit pressurization fixed at about 7 MPa. In the PWR design, the water is highly pressurized to 12.3–16 MPa in order to avoid bulk boiling all along the fuel assembly height, possibly allowing only very local nucleate boiling around the hot spots. At a pressure of 15.5 MPa, the water boiling temperature is about 345°C. A typical maximum temperature at normal operation is 326°C at the core exit, compared to somewhat less than 290°C in a BWR.

Uranium dioxide is the most well known and thoroughly optimized fuel material, accounting for the tremendous volume of fuel irradiated during 60 years, and being the subject of crucial experimental programs conducted worldwide, as well as a large number of survey programs. The temperature range of the fuel in the LWR is different from the fast breeder reactors (FBRs) or the PHWRs (pressurized heavy water reactors), ranging only from about 500–1200°C in normal operation. In terms of burnups, it has been demonstrated that UO_2 fuels are able to achieve 100 MWd kgM⁻¹ local pellet average in LWR. In 2019, the batch average discharge burnups approved by some safety authorities ranged up to 70–75 MWd kgM⁻¹, that is, what is technically achievable within the generally accepted 5% enrichment limit. [Fig. 2](#) shows the evolution of the average fuel discharge burnup in the USA. The discharge burnup has increased steadily since the mid-seventies and until approx. 2005 when it stabilized. This saturation is driven by the

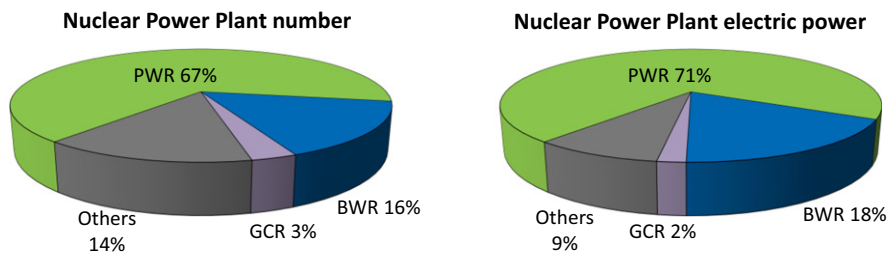


Fig. 1 Distribution of the reactor designs in the nuclear electricity production in 2019. PRIS – Power Reactor Information System (www.iaea.org/pris), © IAEA.

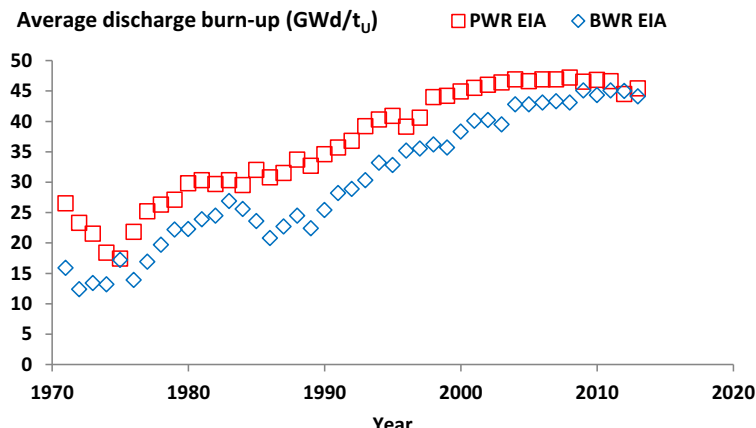


Fig. 2 Evolution of the average fuel oxide discharged burnup from 1971 to 2013 in the USA (U.S. Energy Information Administration statistics – EIA).

extension of cycle lengths, going from 12 month cycles to 18 and 24 month cycles, thus reducing outage costs and increasing capacity (on-line time), but to the detriment of fuel utilization, i.e., average discharge burnup for a given initial ^{235}U enrichment.

The optimal discharge burnup depends on technical and economical aspects, which obviously evolve with time.¹ However, in the framework of a closed fuel cycle including spent fuel reprocessing and MOX fuel reloading, it was estimated that 52 MWd kgM⁻¹ (batch average) could be an optimum in order to avoid a too significant degradation of the isotopic composition of the reprocessed plutonium in MOX fuels. Indeed, the higher the discharge burnup of the reprocessed spent fuel, the higher is the proportion of non-fissile plutonium isotopes, curium, and americium.²

This article deals with the basic knowledge and state of the art regarding LWR fuel thermal and mechanical behavior: survey programs, typical assembly and rod designs, operating conditions, and trends in fuel evolution and development. The main phenomena occurring in the LWR oxide fuels are described, focusing on irradiation conditions and long-term effects of irradiation on material properties, in particular microstructure evolution. Control of fuel cladding integrity, that is, fuel reliability, is then discussed.

For in-depth information on LWR oxide fuel's behavior and performance, we recommend Olander³ and Bailly *et al.*⁴

2.02.2 Experience of Oxide Fuel in LWRs

2.02.2.1 History of Development

After the Second World War, engineers began to develop methods to use nuclear energy for propulsion and the generation of electricity. On 20 December 1951, the Experimental Breeder Reactor-I (EBR-I) produced the first electricity in Idaho,⁵ powering electric light bulbs under the leadership of Walter Zinn. This was the first electricity produced with nuclear energy, followed by the advent of the nuclear submarines. The PWR design was first developed for submarine applications, but was soon adopted for commercial energy production. Zirconium alloys were primarily used because of the minimal interaction of zirconium with thermal neutrons, allowing a higher reactivity of the core and a reduction of the core size to reach criticality for a given ^{235}U enrichment. In the United States, the first nuclear plant to be connected to the commercial electricity grid was the Shippingport unit, built in Pennsylvania by the federal government's Atomic Energy Commission together with Admiral Rickover's navy organization. The plant was able to produce 150 MWe. The first full power commercial PWR was designed by Westinghouse and built for the Yankee Atomic Power Corporation at Rowe, MA, producing 250 MWe; it was in operation from 1958 to 1991. In the meantime, the Argonne National Laboratory had developed the BWR concept. In 1960, Commonwealth Edison started operation of the first commercial BWR at Dresden, IL, designed and built by General Electric, with a production capacity of 250 MWe.

Other concepts were developed at the same time by other countries such as GCRs in France and United Kingdom (MAGNOX), HPWRs in Canada, and VVER (a special type of PWR) and RMBK in Russia. The 1950s and 1960s was the first period for utilities to get acquainted with owning and operating nuclear plants. Encouraged by the first successes and facing a large increase in electricity consumption, utilities started to look for more extensive nuclear production. After the 1973 oil crisis, the motivation was the highest for countries having little or no domestic fossil fuel production. At this time, several of these countries invested heavily in nuclear electricity production, for example, France, Belgium, Japan, and Sweden. Because of the simplicity of the concepts, and probably also due to the large experience acquired with nearly 100 units in the United States, LWR designs were chosen to produce nuclear electricity at a larger scale. The main nuclear plant providers in the West for PWR were Westinghouse, Combustion Engineering, KWU (Germany) and Babcock & Wilcox, and for BWR, General Electric and ASEA-Atom. Westinghouse and General Electric gave licenses to several European and Japanese companies. This is the main reason for the consistency of most of the western LWR fuel designs. In the meantime, in the Soviet Union, VVER reactors were developed and refined by OKB Gidropress.

Westinghouse was first providing PWR units with an electric power generation level of about 900 MWe. The 1300 MWe level was achieved at the end of the 1970s and 1450 MWe level in the 1990s. The Soviet Union followed the same trends with some delay. The change of scale was mainly obtained by an increase in the number of fuel assemblies as well as their length. However, enlarging the core imposed adaptations of the core management and the mode of operation to guarantee radial core stability.

In the 1970s, based on the large US and Soviet Union-acquired experience, LWR fuel was already well optimized to attain maximum assembly burnups of around 35 MWd kgM⁻¹, with a PWR core management by a third of the core. A large research and development investment has since been made worldwide, to increase the discharge burnup, optimize the nuclear fuel cycle, and to enhance fuel reliability. Programs were initiated to:

- Improve the UO_2 fuel density stability, leading to preferred powder manufacturing processes: The Integrated Dry Route developed by BNFL, and the wet routes, ammonium diuranate (ADU) and ammonium uranyl carbonate (AUC).
- Limit the risk of fuel rod failure by pellet-clad mechanical and chemical interaction, by imposing limits on the linear heat generation rate, as well as through the rod diameter reduction following the transition from 14×14 to 17×17 lattices, and by improving the plant operation management.
- Limit the risk of failure caused by migrating debris (e.g., steel wire fragments) in the primary circuit, by improving plant working practices, and by adding a filter at the assembly bottom end.
- Justify the load follow operating conditions necessary when nearly 80% of the electricity production is nuclear (France and Belgium).
- Limit the fuel rod bow and the PWR fuel assembly deformation, to facilitate assembly reloading and avoid gap pitching between fuel rods; modification of the spacer grids and mixing grids to increase the assembly rigidity.

Table 1 List of the main international programs conducted on LWR fuel between 1970 and 2019

Project	References	Period	Subject
OVER-ramp	6	1977–1983	PCI/PCMI
SUPER-ramp	7	1980–1983	PCI/PCMI
DOE/Petten	8	1983–1984	PCI/PCMI
TRIBULATION		1984–1987	Fuel rod behavior after a transient
HBEP	9,10	1979–1988	Fission gas release at high burnup and high burnup fuel transformation (HBS)
HBC	Several progress reports	1987–1994	Fuel chemistry
NFIR I	Large number of proprietary reports	1982–1988	Global fuel behavior at high burnup
ROPE-I	http://www.nea.fr/abs/html/nea-1722.html	1986–1993	BWR rod overpressure experiments
ROPE-II	http://www.nea.fr/abs/html/nea-1723.html	1991–2008	PWR rod overpressure experiment
NFIR II	Large number of proprietary reports	1988–1994	Fuel rod behavior under irradiation – fuel and cladding properties
NFIR III	Large number of proprietary reports	1992–1999	Fuel rod behavior under irradiation – fuel and cladding properties
HBRP	11–14	1994–2002	High burnup structure (HBS or RIM)
NFIR IV	Large number of proprietary reports	1998–2004	Fuel rod behavior under irradiation – fuel and cladding properties
HBRP_NT	15	2002–2007	High burnup structure (HBS or RIM)
NFIR V	Large number of proprietary reports	2004–2010	Fuel rod behavior under irradiation – fuel and cladding properties – fuel dispersion
NFIR VI	Large number of proprietary reports	2010–2016	Continuation of the NFIR program
NFIR VII	Ongoing	Started in 2016	Continuation of the NFIR program
NXO	16	2006–2009	Multiscale approach of HBS
F-BRIDGE	https://cordis.europa.eu/project/rcn/88393/results/en	2008–2012	Acquisition of basic data for modeling and multiscale approach
SCIP (Studsvik Cladding Integrity Program)	Studsvik,	2004–2009	PCI/PCMI and hydrogen-assisted cladding failure modes
SCIP-2	Studsvik,	2009–2014	Continuation of SCIP, focusing on pellet behavior
SCIP-3	Studsvik	2014–2019	Continuation of SCIP, focusing mainly on fuel behavior in a LOCA scenario
SCIP-4	Studsvik	Starting in 2019	
OECD Halden Project	Large Number of reports	Irradiation program terminated in 2018 due to closure of test reactor	Extensive irradiation experiments using instrumented fuel
REPNa (Cabri)	17,18	1992–2000	RIA
CIP (Cabri)		2000 – ongoing	RIA

- Reducing BWR assembly bow by optimizing the materials used for the channel box, as well as fine-tuning the manufacturing processes.
- Increase the batch discharge burnup up to 60 or 70 MWd kgM⁻¹ which requires a detailed understanding of material properties and microstructure evolution with irradiation, in particular, the behavior of the gaseous and volatile fission product species in UO₂.
- More generally, improve our understanding and modeling of materials, together with our insights into the mechanical assembly and rod structure behavior under irradiation. In order to cope with the needs to increase the operational margins and flexibility, fuel material evolutions were investigated.
- By adding “burnable” neutron-absorbing elements to limit the core reactivity at the fuel's beginning of life (gadolinium, erbium, or boron).
- By adding chemical species such as niobium, chromium, and alumino-silicates to increase the grain size and delay the fission gas release during normal operation and/or power transients. Such additives can also influence the viscous properties at medium temperatures, that is, improve the pellet-cladding mechanical interaction (PCMI) behavior.

Moreover, a large number of research projects have been focused, mainly since the 1980s, on the recycling of plutonium. The particular behavior of these heterogeneous MOX fuels will be described in this article as well, focusing on their specificities.

In terms of international research projects, since the 1970s, the classification can be made in several large categories: power ramps (PCI/PCMI in power transients or accidents), fission gas behavior and high burnup structure (HBS), fuel chemistry, fuel properties evolution with burnup (conductivity, specific heat, mechanical properties, swelling and densification, fuel stability), cladding behavior (in-pile and out-of-pile creep, growth, corrosion, and hydrogen pickup). Major reference programs are given in **Table 1**.

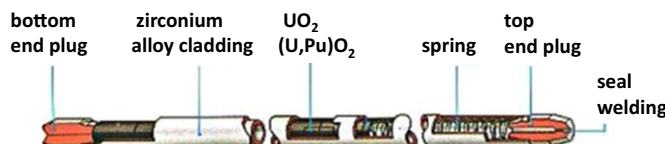


Fig. 3 Fuel rod scheme.

Table 2 Main fuel rod characteristics for current PWR and BWR plants

Fuel rod characteristics	PWR 17 × 17	VVER	BWR 8 × 8	BWR 10 × 10
Fuel rod outer diameter (10^{-3} m)	9.45	9.1	12.30	9.6–9.8
Cladding inner diameter (10^{-3} m)	8.347	7.8	10.68	9.0–9.2
Cladding wall thickness (μm)	570	650	810	Around 600
Cladding material	Zirconium alloy	E110	Zry-2	Zry-2
Pellet diameter (10^{-3} m)	8.19	7.6	10.4	8.2–8.5
Central hole diameter (10^{-3} m)	–	0/1.2	–	–
Pellet length (10^{-3} m)	10–12	9–12	10.4	Around 10
Fuel	UO ₂	UO ₂	UO ₂	UO ₂
Possible neutron absorbent additives	Gd, Er, B	Gd	Gd	Gd
Initial ^{235}U enrichment (%)	3.2–5	3.8–5	3.2–5	3.2–5
Theoretical density (kg m ⁻³)	10,950	10,970	10,950	10,950
Fuel initial porosity (%)	3–7	2.2–5	4.5–7	3–5
Fuel initial relative density	0.93–0.97	0.95–0.977	0.93–0.955	0.95–0.98

2.02.2.2 Fuel Elements Design

The PWR and BWR fuel assembly designs have progressively evolved with time. However, these designs approached maturity in the 1970s with 17×17 square mesh structures for most western PWR fuel and in the 1990s for BWR with 10×10 lattices. Later developments include the 18×18 lattice for KWU PWR fuel, and 11×11 lattice BWR fuel from AREVA and Westinghouse. From the beginning, VVER fuel has been characterized by a hexagonal mesh structure, involving 127 positions in the originally 440 MWe VVER-440, and later 331 positions in the 1000 and 1200 MWe VVER-1000 and VVER-1200 standardized designs, with 9.1 mm cladding outer diameter equivalent to some modern PWR designs.

More recent evolutions were focused on the rigidity of the structure in western PWR and VVER assemblies, enhancing the neutron economy in BWR assemblies, and fuel reliability, for example, protection against migrating objects in the coolant ('debris') and increasing the margin to pellet-cladding interaction (PCI) failure in BWR fuel. Materials have also evolved to enable increasing burnups and reduce geometric deformation during operation. LWRs are able to operate with MOX fuel in order to recycle plutonium. Europe and Japan have irradiated such MOX fuel at a large scale in PWR units.¹⁹

The fuel rod is a zirconium alloy tube (the cladding), containing UO₂ or MOX cylinders ('pellets') piled to form the fuel stack, with a remaining upper volume called plenum at the top (see Fig. 3), to allow fuel stack elongation and accommodate the released gaseous and volatile fission products. The fuel stack is typically maintained during handling operation by a spring placed in the plenum. The fuel rod is closed at both ends by sealed end plugs after filling it with a neutral gas (helium) with a pressure ranging from 1 to 34.5 bar (0.1–3.45 MPa), depending on the design. The primary purpose of the fill gas is to facilitate heat transfer from the fuel stack to the cladding, hence the choice of He with its low atomic weight. In addition, PWR fuel rods are pressurized to partly counterbalance the primary circuit pressure (12.3–16 MPa for PWR versus 7 MPa for BWR), i.e., to delay creep down of the cladding. However, the fill pressure has been progressively reduced with increasing discharge burnups (general trend in the core management), in particular with MOX fuel, to avoid exceeding the pressure criterion at end of life. The initial (fill) pressure is between 1.5 and 2 MPa for more recent PWR fuel fabrications, and 0.2–0.8 MPa for BWR fuels.

Table 2 provides the main characteristics of fuel rods. PWR data are given for the 17×17 design, which is the most common, and VVER-1200. For BWRs, the standard has evolved over 8×8 and 9×9 to a 10×10 lattice.

2.02.2.2.1 The fuel pellets

Fuel pellets are manufactured from uranium dioxide powders (or (U,Pu)O₂ powders) by a pressing process followed by sintering at high temperature (e.g., 1740°C) in a controlled atmosphere for several hours. Manufacturing conditions have been empirically optimized during the 1960s and 1970s. These processes lead to a ceramic material containing an initial porosity ranging from 2% to 7% of the volume (Fig. 4). When necessary, pore formers are used. The final density ranges from 10.2 to



Fig. 4 UO₂ pellets.

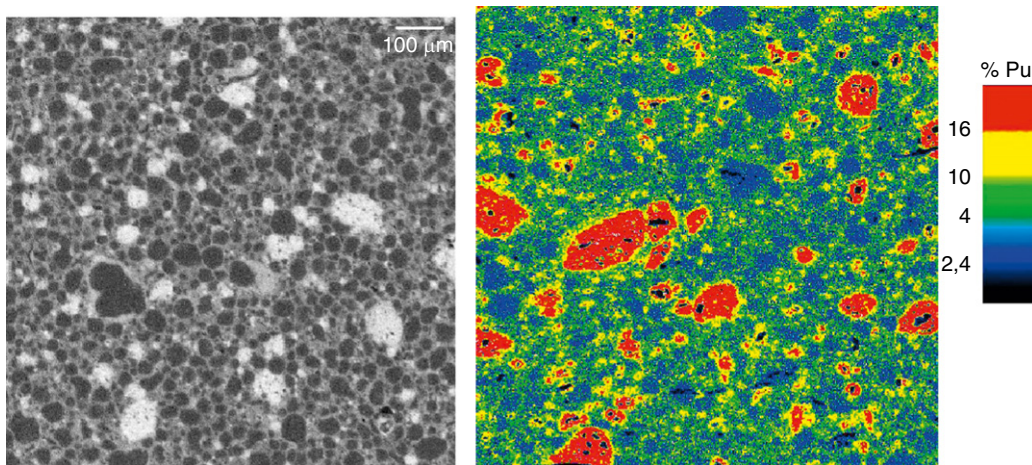


Fig. 5 Plutonium EPMA maps in a fresh mixed oxide fuel (MOX).

10.7 g cm⁻³, a typical UO₂ theoretical density being 10.95 g cm⁻³. The average grain size usually ranges between 8 and 30 μm. The fuel pellets are generally designed with end dishes to reduce the pellet stack axial thermal expansion and reduce PCMI in case of a power transient. They are also generally designed with chamfers, to reduce corner defects, to facilitate loading into the tubing, and to reduce PCMI.

VVER fuel pellets are traditionally manufactured with a central hole of currently 1.2 mm diameter (annular or hollow pellets) without dishes, but the need for more economic designs has recently lead to the introduction of solid pellets as well.

The industrial MOX fuel fabrication is generally done by a two-step mixing process initially developed by Belgonucleaire, and improved more recently to better homogenize the plutonium distribution. A first blend, called "master blend", is produced, mixing plutonium oxide with depleted uranium oxide. In the present fabrications, the plutonium content in this master blend is close to 30%. In a second step, this master blend is mixed again with depleted uranium oxide to obtain the targeted average plutonium content, typically between 6% and 10%. After pressing, the 'green' pellets are sintered in a controlled atmosphere at ambient pressure. This aims to reach a 2.000 O/U stoichiometry. The final material is obviously heterogeneous, as shown in the electron probe microanalysis (EPMA) picture in Fig. 5. The average grain size is smaller than in UO₂ fuels, particularly in the plutonium-rich agglomerates.

The isotopic composition of the transuranics (²³⁸Pu, ²³⁹Pu, ²⁴⁰Pu, ²⁴¹Pu, ²⁴²Pu, ²⁴¹Am, ²⁴²Cm) depends upon the final discharge burnup of the reprocessed fuel. The isotopes ²⁴⁰Pu, ²⁴²Pu, and ²⁴¹Am are neutron absorbers, i.e., degrade the fissile quality of the plutonium.

Plutonium is produced during irradiation as follows:

- ²³⁹Pu production by neutron absorption in ²³⁸U, followed by β-decay (²³⁹Pu half-life 24,000 years, ²³⁹Np half-life 2.36 days)
 - $^{238}U + {}_0^1n \Rightarrow {}_{93}^{239}Np \rightarrow {}_{94}^{239}Pu + \beta^- + \gamma$
- ²⁴⁰Pu production by neutron absorption in ²³⁹Pu (²⁴⁰Pu half-life, 6563 years)
 - ${}_{94}^{239}Pu + {}_0^1n \Rightarrow {}_{93}^{240}Pu$
- ²⁴¹Pu production by neutron absorption (²⁴¹Pu half-life, 14 years)
 - ${}_{94}^{240}Pu + {}_0^1n \Rightarrow {}_{93}^{241}Pu$
- ²⁴¹Am production by β-decay (²⁴¹Am half-life, 432 years)
 - ${}_{94}^{241}Pu \rightarrow {}_{95}^{241}Am + \beta^- + \gamma$ and ${}_{95}^{241}Am \rightarrow {}_{93}^{237}Np + {}_2^4He + \gamma$

Table 3 Decay characteristics for the different isotopes

Isotopes	Half-life (years)	Decay constant (s^{-1})	Activity per gram of Pu (Bq)	Decay product	Mode	Decay energy (MeV)	Energy (W/g Pu)
^{238}Pu	87.74	2.505E – 10	6.340E + 11	^{234}U	α	5.593	5.679E – 01
^{239}Pu	24,110	9.116E – 13	2.297E + 09	^{234}U	α	5.245	1.930E – 03
^{240}Pu	6563	3.349E – 12	8.405E + 09	^{236}U	α	5.140	6.919E – 03
^{241}Pu				^{241}Am	β^-	0.021	1.287E – 02
	14.35	1.532E – 09	3.828E + 12	^{237}U	α	5.140 (0.025%)	
^{242}Pu	375,000	5.861E – 14	1.459E + 08	^{238}U	α	4.984	1.164E – 04
^{241}Am	432.2	5.086E – 11	1.271E + 11	^{237}Np	α	5.638	1.148E – 01

^{241}Am production by neutron absorption (^{242}Am half-life, 16.02 h), then ^{242}Cm (half-life 160 days) and ^{242}Pu (half-life 3.76×10^5 years) by β^- or β^+ -decay

○ For 82,7%: $^{95}\text{Am} + {}_0^1n \Rightarrow {}_{95}^{242}\text{Am} \rightarrow {}_{96}^{242}\text{Cm} + \beta^- + \gamma$

○ For 17,3 %: $^{95}\text{Am} + {}_0^1n \Rightarrow {}_{95}^{242}\text{Am} \rightarrow {}_{94}^{242}\text{Pu} + \beta^+ + \gamma$

^{238}Pu production by α -decay (^{238}Pu half-life, 87.74 years)

○ ${}_{96}^{242}\text{Cm} \rightarrow {}_{94}^{238}\text{Pu} + {}_2^4\text{He} + \gamma$

All these isotopes are, or decay into, α -emitters. Their decay properties are given in **Table 3**.

As a consequence, the americium content of unirradiated MOX fuel increases with time.

The production of helium in MOX fuel is much higher than in UO₂ fuel, due to the alpha decay of transuranic isotopes. It cannot be neglected in fuel rod behavior simulation, since it may contribute significantly to the fuel rod inner pressure during and after irradiation. Notably, some helium will be produced by alpha decay also after completed irradiation, and must be considered when predicting rod pressure in intermediate and final storage scenarios. Nevertheless, the helium volume measured in the plenum after rod puncturing is often somewhat lower than the helium volume introduced as fill gas during fabrication. Helium is absorbed by the fuel at low burnup and remains there, together with He generated during irradiation, partly in solution and partly in the as fabricated pores.²⁰⁻²²

2.02.2.2.2 The fuel rod cladding

The cladding material is normally a zirconium alloy, traditionally Zircaloy-2 for BWR fuel, Zircaloy-4 for western PWR and E110 for VVER. However, alloys with improved in-reactor performance, in particular with respect to corrosion and hydrogen pickup, are also used for modern fuel (ZIRLO™ and M5™ for PWR, and ZIRON™ and HiFi™ for BWR). The main differences are the presence of nickel in Zircaloy-2 while not in Zircaloy-4 or E110, and of niobium in E110, ZIRLO and M5. ZIRON and HiFi are characterized by an iron content above the ASTM range for Zircaloy-2, but are otherwise similar to the latter. For Zircaloy-4 and ZIRLO, the Sn content is a key parameter to control the corrosion rate. Another important manufacturing parameter, impacting cladding microstructure and mechanical properties (strength, creep, irradiation growth) is the final heat treatment, which varies between materials and manufacturers. Depending on the final anneal, the material obtained may be stress relieved (SRA or CW, cold worked), partially recrystallized, (pRXA) or fully recrystallized (RXA).

Since control rods are deployed during normal operation of a BWR, and movements of those control rods lead to large and rapid changes of local power, PCI is a significant mode of rod failure for BWR fuel, relatively common throughout industry history. Modern BWR cladding is therefore usually equipped with a liner barrier of a dilute Zr alloy on the inner wall, to protect against this failure mode.

2.02.2.2.3 Use of additives in the fuel

A number of rods in a fuel assembly usually incorporate a burnable neutron absorber, which is typically either boron, with boron-10 the active isotope, or gadolinium, where gadolinium 155 and 157 are the burnable neutron poisons. These serve to limit the fuel reactivity at the beginning of life, to limit power peaking, and furthermore

- For PWR, to limit the effluent production by using excessive boric acid volume in the primary circuit.
- For BWR, to extend the lives of control rods which would otherwise need to be deployed to control excess reactivity.

New fuel types were also developed, featuring additives such as niobium, chromium, and alumino-silicates to increase the as-fabricated fuel grain size, and consequently, slow down the fission gas release kinetics. Such additives can simultaneously provide other benefits, for example, higher density, reduced densification, and a better PCI behavior. In the case of MOX MIMAS (Micronisation Master blend) fuels, adding chromium to fabrication operations may also contribute to improved homogenization of plutonium in the fuel.²³⁻²⁵

2.02.2.2.4 The fuel rod assemblies

The fuel rods are bundled into fuel assemblies, with examples shown in (Fig. 6). Main characteristics, representative for typical current designs, are given in **Table 4**.

For both western LWR types (PWR and BWR), fuel assemblies are square-meshed structures, while for VVERs they are hexagonal. In western PWRs, the number of fuel rods per assembly has evolved between the 1960s and the 1970s. 12×12 became

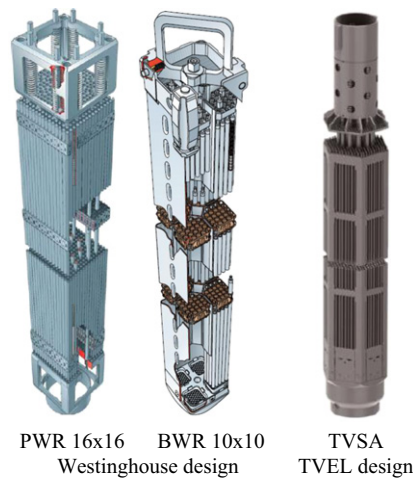


Fig. 6 Fuel rod assemblies, pictures from Westinghouse and TVEL companies.

Table 4 Main fuel core characteristics for modern PWR and BWR plants

Power plant type (MWe)	PWR 900	PWR 1300	PWR 1400	VVER-440	VVER-1000	Typical BWR
Number of fuel assemblies in the core	157	193	214	349	163	700–900
Type of assembly	17 × 17	17 × 17	17 × 17	Hexagonal	Hexagonal	10 × 10
Number of water rods	25	25	25	1	19	
Number of fuel rods per assembly	264	264	264	126	312	91–96
Total number of fuel rods in the core	41,448	50,952	56,496	43,974	50,856	63,000–86,000
Primary circuit coolant and moderator	Light water					
Primary circuit pressure (bar)	155	155	155	123	290	~70
Feed coolant temperature	285	285	285	267	305	~286
Average coolant temperature (°C)	300	300	300	282	4.57	~4
Assembly length (m)	4.00	4.50	4.50	3.22	3.53–3.68	~3.7
Active fuel length (m)	3.66	4.268	4.268	2.48		

14 × 14, and 15 × 15 became 17 × 17, while retaining the same outer dimensions. One design even uses an 18 × 18 lattice. Simultaneously, the fuel rod external diameter decreased from 1.051 to 0.951 cm to improve the core physics design, decrease the linear heat generation rate and thereby the fuel centerline temperature, while maintaining a similar assembly power. The original 15 × 15 PWR assembly had a channel box like that of BWR fuel. It was eliminated to facilitate the thermohydraulic cross flow between fuel assemblies, thus reducing the risk to reach locally the critical heat flux leading to a departure from nucleate boiling (DNB). In addition, this led to a reduction of parasitic absorption (in the channel) and a reduction of the potential consequences of coolant flow blockage in an assembly.

In VVER, the assembly is hexagonal and comprises 127 positions for VVER-440 reactors and 331 for VVER-1000 and VVER-1200 reactors. VVER-440 assemblies are typically equipped with a shroud (channel box) made of Zr-2.5%Nb alloy. A unique feature of VVER-440 reactors is that reactivity is controlled by means of control assemblies, attached to the top of specific fuel assemblies called follower assemblies. As the control assemblies are lowered into the core, the follower assemblies go beneath the core. They therefore show very specific axial burnup profiles (see Fig. 7).

The BWR assembly has evolved from 6 × 6 and 7 × 7 over 8 × 8 and 9 × 9 lattices to the modern 10 × 10 mesh designs. More recently, 11 × 11 designs are being introduced. The fuel assembly is equipped with a channel box made from a zirconium alloy, providing mechanical and thermohydraulic insulation from neighboring assemblies. This feature has facilitated large improvements in key performance parameters over the years, for example, by means of the above-mentioned evolution of the lattice mesh, and by adding internal structures such as water rods or a water cross.

2.02.2.3 LWR Operating Conditions

2.02.2.3.1 PWR normal operating conditions

The LWR fuel rods are designed to operate at medium heat rate, ranging from 15 to 25 kW m⁻¹ (150–250 W cm⁻¹). In 17 × 17, 16 × 16 and VVER designs, these linear heat rates lead to a fuel centerline temperature not exceeding 1000–1200°C. This is fundamentally different from the FBR fuel regarding fission gas release, i.e., with a low activation of thermal gas diffusion during

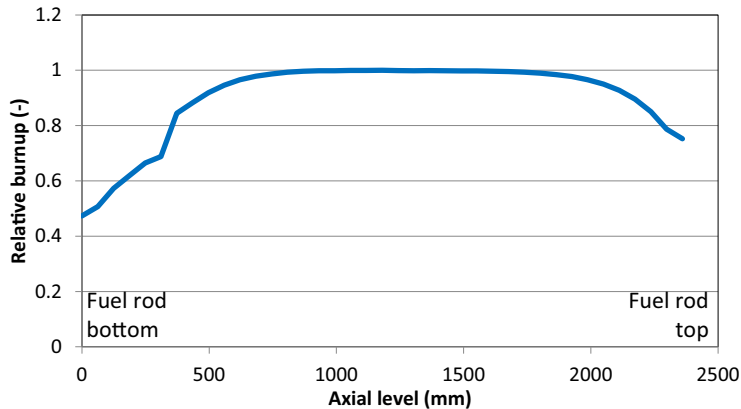


Fig. 7 Burnup profile of a follower rod in a VVER-440 control assembly (burnup: 47 MWd kgM^{-1}).

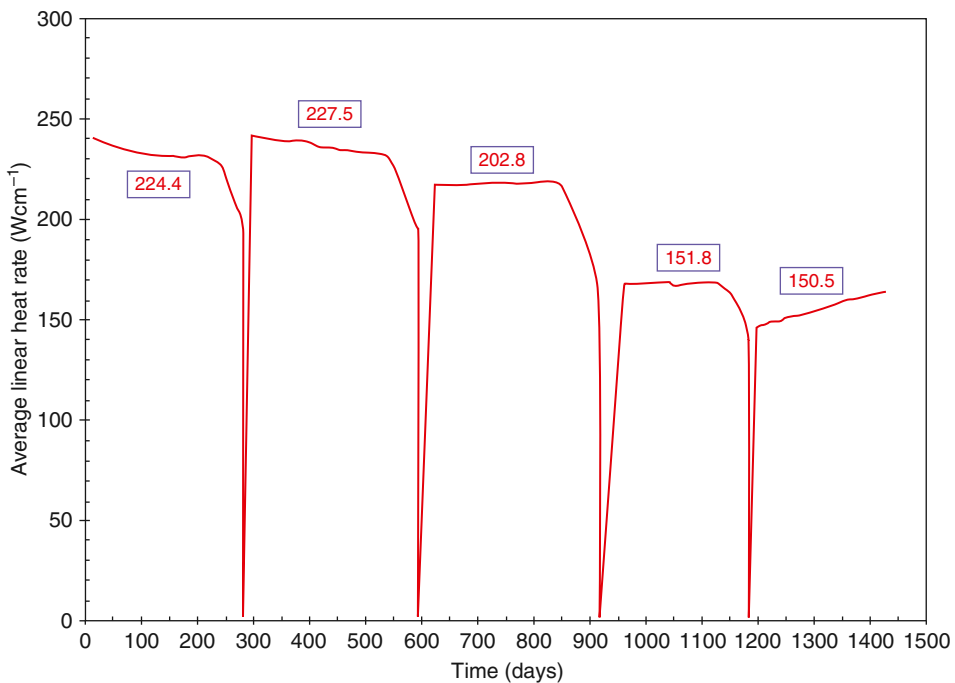


Fig. 8 Evolution of the linear heat rate in base irradiation for standard pressurized water reactor UO_2 fuel.

normal operation. Another characteristic for PWR fuel is the very uniform neutron spectrum, all along the assembly height, given that the moderator (primary circuit water which plays the role of coolant as well) remains essentially in the liquid phase at all axial levels. The inlet core coolant temperature is typically around 285°C and the increase from the bottom to the top is around 40°C . This temperature difference has a slight effect on the moderator efficiency. When local boiling occurs, it stays localized near the fuel rod cladding surface. The water saturation temperature at a pressure of 15.5 MPa is 345°C and the maximum core outlet temperature in normal operation is around 326°C . The fuel assembly pressure drop is around 1.5 MPa.

The maximum linear power at the beginning of the core cycle is located near the bottom, and shifts to the upper part of the assembly as irradiation proceeds. The axial power profile shows a peaking factor ranging between 1.08 and 1.2. The control rods are never deeply inserted during normal operation of a PWR. **Figs. 8 and 9** show typical average power histories for a standard UO_2 fuel rod irradiated for five annual cycles, and for a standard MOX fuel irradiated for four annual cycles, respectively. The power generated in the fuel rod, highest during the two first cycles, generally decreases with time as UO_2 reactivity decreases with burnup (fissile atoms consumption). In the MOX fuel, the global reactivity does not decrease so fast: power during the second and third cycles is close to the first cycle's power. The fourth cycle depends upon the location of the MOX assembly in the core. Due to their relatively high production of fast neutrons (compared to UO_2 fuel), MOX assemblies are managed so as to avoid positions close to the core vessel. **Fig. 10** shows an example of the final burnup axial profile, obtained by γ -scanning. In this example, the power peaking factor is 1.084 and the maximum burnup occurs at 2640 mm from the lower end of the rod.

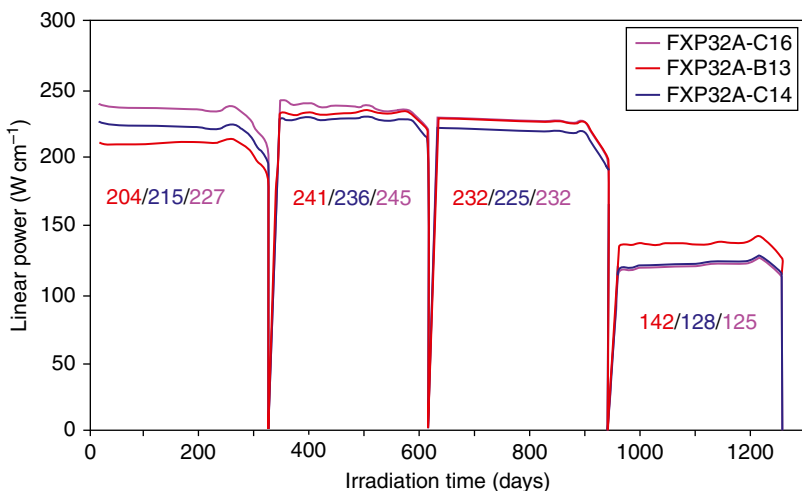


Fig. 9 Evolution of the linear heat rate in base irradiation for standard pressurized water reactor mixed oxides fuel.

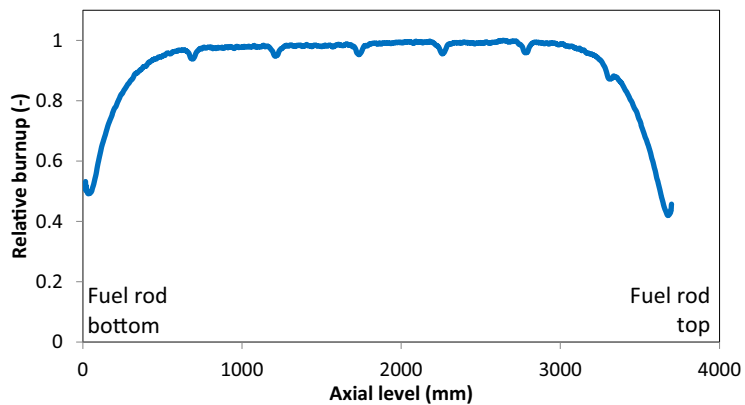


Fig. 10 Final burnup axial profile for a pressurized water reactor fuel rod.

France has a high proportion of nuclear electricity production (about 80%), and therefore, a certain number of the Electricité De France (EDF) nuclear reactors must adjust production such that it matches electricity demand. These usually operate in so-called “load follow” (daily cycles, decreasing power to 30% or 50% of the nominal value during the night) and frequency control (instantaneous adaptation to the grid in a range of $\pm 5\%$ around nominal power). Semi-absorbent control rods (so-called ‘gray rods’) are inserted to enable these power variations. Such semi-absorbent control rods also help limiting the ^{135}Xe isotope poisoning effects. It was demonstrated that such power cycling has only a slight influence on the overall fuel performance, even when considering that local power cycling may be higher than the average power variations. However, if the reactor spends too much time at reduced power, fuel rods undergo so-called “deconditioning”. This occurs when the pellet-cladding gap reopens at lower power (due to thermal contraction of the pellet), and the cladding has time to creep down significantly, thereby reducing the margin to PCMI failure.

2.02.2.3.2 BWR normal operating conditions

One key difference between the core physics in a BWR reactor compared to a PWR, apart from the lower system pressure, is the effect of the relative void (steam) volume in the boiling water, gradually increasing from the bottom to the top of the core. The void induces a significant neutron sub-moderation resulting in a PWR-like spectrum at the bottom of the core and a harder spectrum in the upper part. This leads to significantly more generation of fissile nuclides in the upper part, and hence, an axial power profile that depends on the burnup of the fuel assembly ([Fig. 11](#)).

Net boiling, starting near the bottom of the core, leads to a constant coolant temperature of around 286°C , that is, significantly less than in the upper parts of a PWR core. The core power is controlled using cruciform control blades, inserted between fuel assemblies, which are equipped with channel boxes. This leads to a more non-uniform power distribution, both radially and axially, than for a PWR, where usually all control rods are withdrawn during operation and core power is controlled using boron in the coolant. The impact of control blades is evident from [Fig. 12](#), where we see significant differences between individual fuel rods (at one selected axial position), and step changes in power, in particular during the first cycle.

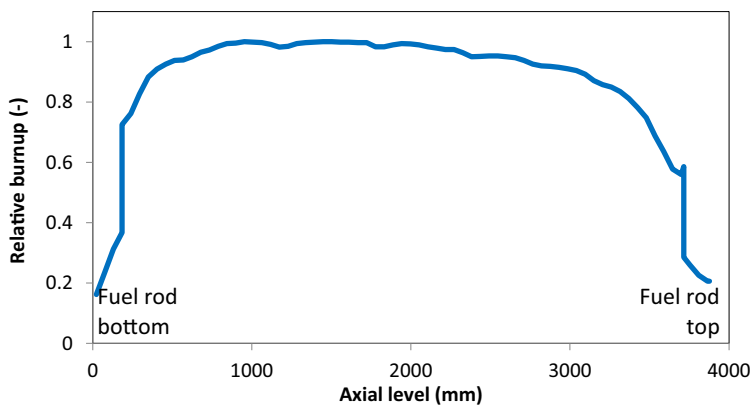


Fig. 11 Example of a burnup axial profile for a high burnup boiling water reactor fuel rod. Note that the rod has low-enrichment zones ('blanket zones') at both ends, for increased neutron economy.

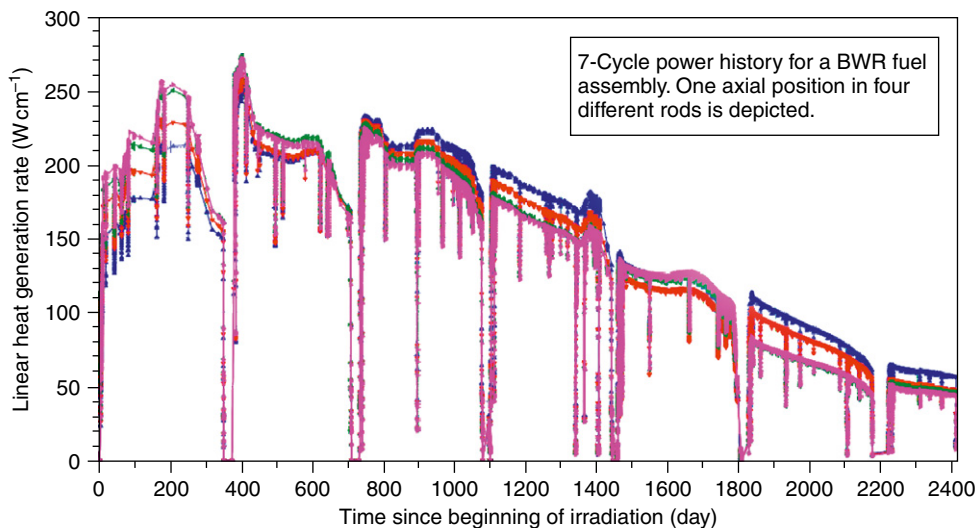


Fig. 12 Example of a boiling water reactor power history. Courtesy of KKL.

2.02.3 Behavior at Beginning of Life

2.02.3.1 Basic Irradiation Effects

First, one has to keep in mind that as soon as the irradiation of the fuel starts, the fuel pellets evolve to accommodate the in-pile conditions. For this, there are two drivers:

- The local temperature
- The fission energy

For the portion of fuel operating at temperatures lower than 800°C (pellet periphery), the second source is predominant. On the other hand, in the pellet center, the temperatures are high enough to activate diffusion mechanisms driven by Brownian mobility. The fission energy is mostly transmitted to the fission fragments in the form of kinetic energy. The average energy is about 60–140 MeV. Then the fission fragments are progressively slowed down, transferring their kinetic energy to the surrounding material, mainly by external atomic electronic layer friction at high energy and then progressively by collision cascades as velocity is decreasing. These cascades induce creation of Frenkel pairs or Schottky defects (U or Pu + 2 Oxygen). Most of these defects are recovered quickly. Souillard²⁶ has estimated, in his Ph.D. thesis, that about 26,500 uranium vacancy-interstitial Frenkel pairs are created per fission, together with 72,700 oxygen vacancy-interstitial pairs. In a standard fuel operating regime, at around 220 W cm⁻¹, each heavy atom (U or Pu) is displaced almost 0.4 times a day. Due to their lower weight, the number is three times higher for oxygen atoms. Since the fuel material is a ceramic, Frenkel defects are electrically charged. The oxygen is then redistributed in a way reflecting electrical symmetries.

Defect recovery is influenced by fission cascades as well as the local temperature and local fission density energies. In the external part of the fuel pellet, the temperature is not high enough to activate atomic diffusion. However, the cascades allow a partial recovery. In a first phase, the overall balance leads to a stabilization of the lattice parameter after a few days of irradiation with the formation and accumulation of dislocation loops.²⁷ At high burnup, this population of dislocation loops is progressively tangling and clustering,²⁸ leading to a material transformation described later in this article (Section 2.02.4.5). At the pellet center, the temperature allows a higher recovery of the irradiation defects. At high burnup, with the general decrease of the fuel linear heat rates, effects of defects accumulations are found and will also be described in Section 2.02.4.5.

2.02.3.2 Thermal Aspects

Generally speaking, the heat equation to solve is:

$$\rho \cdot C_p(T) \cdot \frac{\partial T}{\partial t} - \text{div}(k(T) \cdot \vec{\text{grad}}T) = S(t) \quad (1)$$

where $C_p(T)$ is the local heat capacity of the material ($\text{J kg}^{-1} \text{K}^{-1}$), T is the local temperature (K), $k(T)$ is the local thermal conductivity of the material ($\text{W kg}^{-1} \text{K}^{-1}$), and $S(t)$ is the local power generation (W kg^{-1}).

During normal operation, and even more in accident scenarios, the radial temperature gradient is predominant, compared to the axial gradient. For engineering purposes, the problem can therefore be solved by a one-dimensional finite element calculation, along a radius considering the fuel rod as an axisymmetric structure. The conductivity integral can then be written as follows:

$$\rho \cdot (r, T, t) \cdot C_p(r, T) \frac{\partial T(r, t)}{\partial t} - \lambda(r, T) \cdot \frac{1}{r} \frac{\partial}{\partial r} \left(r \frac{\partial T(r, t)}{\partial r} \right) = S(r, t) \quad (2)$$

If $\overline{P_V}(t)$ is the average volumetric power in the fuel pellet and $f(r, t)$ the radial power profile, it yields:

$$\rho(r, T, t) \cdot C_p(r, T) \frac{\partial T(r, t)}{\partial t} - \lambda(r, T) \cdot \frac{1}{r} \frac{\partial}{\partial r} \left(r \frac{\partial T(r, t)}{\partial r} \right) = f(r, t) * \overline{P_V}(t) \quad (3)$$

For steady-state conditions, the equation can be reduced:

$$-\lambda(r, T) \cdot \frac{1}{r} \frac{\partial}{\partial r} \left(r \frac{\partial T(r)}{\partial r} \right) = f(r) * \overline{P_V} \quad (4)$$

For the cladding, the second term is close to zero (limited to radiation interactions with the cladding). However, the fuel rod heat transfer problem is much more complex than just solving the standard basic equation above. To evaluate the temperature field in the nuclear fuel rod, several additional phenomena are to be accounted for (Fig. 13):

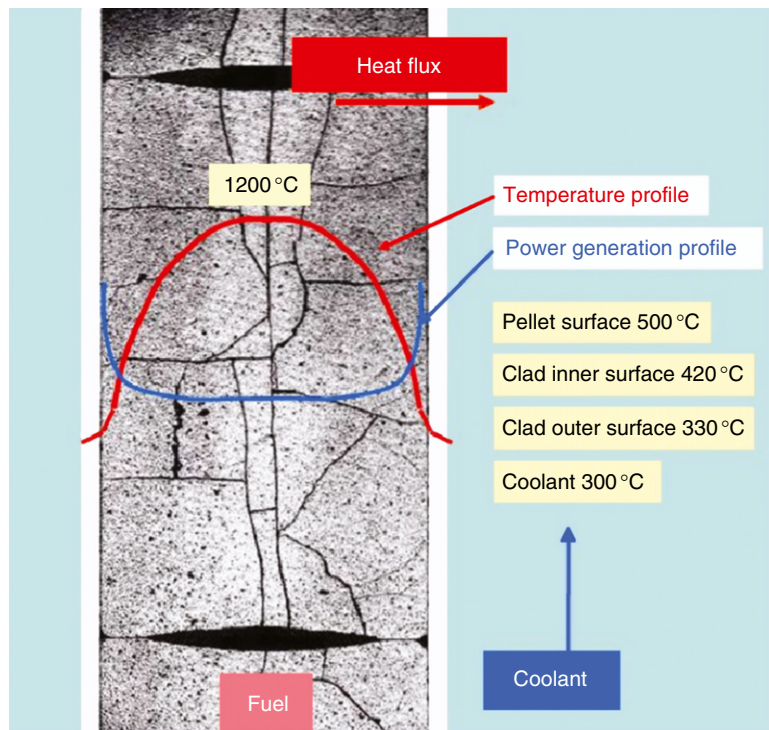


Fig. 13 Temperature profile in light water reactor fuel during base irradiation.

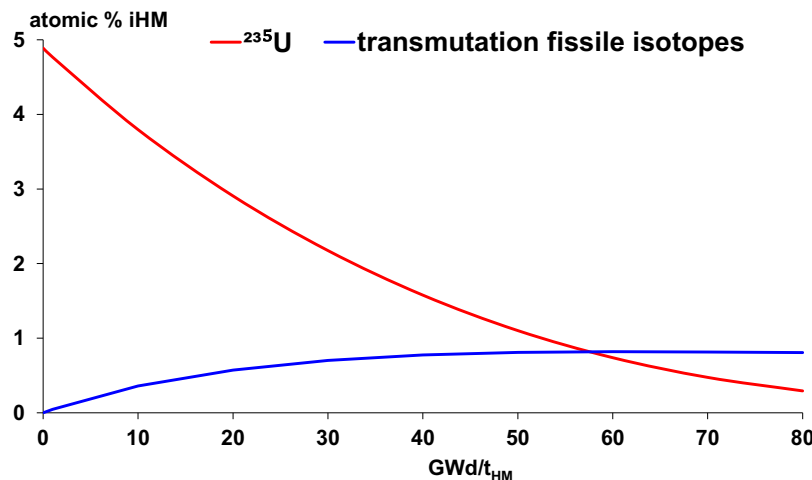


Fig. 14 Increase of transmutation fissile isotope content (mainly plutonium isotopes) with the increasing burnup, while ^{235}U content decreases. Cesar code calculation for a 4.88% ^{235}U enriched UO_2 fuel. Reproduced from Vidal, J.-M., Eschbach, R., Launay, A., et al., 2012. CESAR-5.3: An industrial tool for nuclear fuel and waste characterization with associated qualification. In: Proceedings of the Waste Management Symposia. Phoenix, AR, USA. Courtesy of CEA.

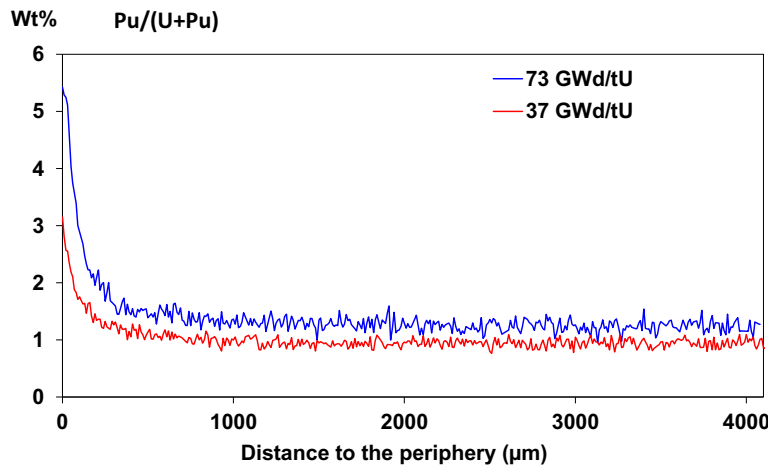


Fig. 15 Electron probe microanalysis, $\text{Pu}/(\text{U} + \text{Pu})$ radial profile for two different average pellet burnups. Courtesy of CEA.

- The radial power generation in the pellet²⁹: The radial power generation is not uniform. At the beginning of the irradiation, the local power is $\sim 10\%$ higher on the pellet periphery, due to self-shielding effect in ^{235}U fissions driven by neutrons entering the rods after interactions in the water (moderator). With increasing burnup, higher local powers are again found on the rim of the pellets, now due to the self-shielding effect of the ^{238}U isotope in the epithermal neutron energy domain. In this domain, the ^{238}U capture cross-section presents very high values for certain neutron energies (resonances). For these energies, the neutron capture probability becomes very high when entering the fuel after slowing down in the moderator. Such capture leads to transmutation of ^{238}U to ^{239}Np , which quickly becomes ^{239}Pu by β -decay (half-life of 2.256 days). The plutonium production is therefore higher in the fuel rim than in the rest of the pellet. Plutonium progressively participates in the energy production, since ^{239}Pu is a fissile isotope; at the same time as the ^{235}U concentration gradually decreases (Fig. 14).

The consequence of the higher plutonium buildup on the rim of the pellets is a progressive shift of power generation towards the radial periphery, which is beneficial as it decreases the centerline temperature for the same overall pellet power generation. An example of the evolution of the radial $\text{Pu}/(\text{U} + \text{Pu})$ profile is given in Fig. 15, for two average pellet burnup values. The radial depletion first increases and then stabilizes as plutonium progressively contributes to the power generation. The details of this evolution obviously depend upon the initial ^{235}U enrichment. In a UO_2 fuel pellet, the lower the initial enrichment, the higher will be the plutonium contribution to power generation. Another, albeit smaller, power generation component is the γ -energy deposition due to photons from the surrounding fuel rods. This deposition can be considered uniform along the radius. (Notably, some of the γ photon energy is deposited directly to the coolant. Similarly, part of the neutron energy is also deposited directly in the coolant). The radial power generation in the MOX fuel is evaluated in the same way, accounting for the different isotopic

composition of this particular fuel. Generally, radial depression is not so prominent in MOX fuel, compared to UO₂. Nevertheless, the same plutonium buildup is observed in the rim due to the ²³⁸U self-shielding. Concerning the axial power distribution, it is generally considered uniform all along the pellet length.

- *The heat transfer between water coolant and cladding wall:* The heat transfer along a heated wall is somewhat complex depending upon the local water state: liquid, local nucleate boiling, formation of a vapor film, bulk boiling, or vapor.³⁰ The water coolant flowing from the bottom to the top of the rod increases its average enthalpy along the cladding.
- The calculation of the temperature drop between the cladding wall and the water coolant is given by:

$$\Delta T = \frac{Plin}{2\pi R_{out} H_{film}} \quad (5)$$

where Plin is the local linear power (W m⁻¹), R_{out} is the cladding outer diameter, and H_{film} is the limit layer conductance (m² W⁻¹ K⁻¹), which depends upon the local regime: forced convection, boiling incipience, partial developed nucleate boiling, bulk boiling, critical heat flux, and vapor.³¹⁻³³ In a PWR, the critical flux corresponds to the DNB regime and the formation of a local and stable insulator vapor film, nearly eliminating heat flux and rapidly leading to fuel failure: The affected fuel segment can actually melt. In a BWR, exceeding the critical heat flux leads to dry-out, a condition where the cladding surface is cooled mainly by flowing steam. The surface temperature increases by several hundred degrees, and after some time (~days), failure can follow by enhanced cladding creep and/or corrosion. Core management specifications and reactor protection systems are obviously designed to avoid reaching such a situation at any location and at any time.

- *Heat transfer through the cladding:* In a first approximation, this can be reduced to heat transfer through a metallic material layer. However, an oxidation reaction occurs with coolant water at the cladding surface, leading to the formation of a ceramic zirconia layer, that is, ZrO₂. Since the thermal conductivity of the oxide layer is much lower than that of the metal, the evolution of the oxide layer is often the dominant factor in the heat transfer analysis. Furthermore, the corrosion rate increases with temperature, that is, at the surface of the metal. Thus, there is a positive feedback between oxide layer thickness and growth rate, in particular in a PWR with its somewhat higher temperature regime. One common design criterion sets a limit to the zirconia layer thickness corresponding to a maximum cladding (metal) wall thickness reduction of 10% (based on ASTM recommendations), corresponding to around 100 μm of oxide.

In addition to the waterside oxide, a thin crud layer is usually found on the cladding surface, caused by the deposition of compounds dissolved in the coolant. These may originate from the reactor primary system (e.g., Fe, Ni, Cu), the source of fresh coolant water (e.g., Si), or represent coolant additives (e.g., Zn, B, Li, K). The thickness and physical properties, in particular thermal conductivity, of the crud varies from plant to plant, depending on the specific coolant chemistry. Needless to say, it is crucial for the reliable operation of fuel to understand and control crud formation.

On the internal cladding wall, a thin zirconia layer can also develop after direct contact with the fuel, that is, starting at medium-to-high burnup levels. The thickness of this layer, when present, is typically around 10 μm. Usually, this oxide layer is neglected in the heat transfer calculation. At high burnup, interaction between the zirconia layer and the pellet surface often leads to bonding and a complex, wavy interface.

- *The heat transfer in the pellet-cladding interface:* In the evaluation of the radial heat transfer, this part is delicate, since the temperature drop through the gap between the fuel pellets and the cladding depends on the gap width, which in turn depends upon the fuel pellet and cladding differential thermal and irradiation-driven expansion/contraction. Moreover, the fuel pellets, first, have no reason to be properly centered within the cladding, and second, cannot be considered as perfect cylinders partly because they crack into several pieces as soon as they are first heated (Fig. 13), and partly because of higher thermal expansions in the hot central part, inducing a general shape of the pellets, with larger diameters at both ends, the so called "hour-glass" shape (see Section 2.02.3.3). (Note that this term "hour-glass", widely used, may seem incorrect to characterize the real pellet shape, considering the pellet end diameter is only a few micrometers larger than the mid-height diameter). Therefore, when the gap is still open, calculations must account for fuel pellet fragments, partially in contact with the cladding and for heat transfer through a gas layer evolving in its composition with burnup. When the gap starts to close, the material surface roughness maintains some minimal gas layer, as long as no bonding occurs. Thus, there are three components of the gap conductance: the convection transfer, the radiative transfer, and the contact conduction. For light gases such as helium or hydrogen, an extrapolation correction is added to the convection transfer to account for the capability of the gas to penetrate into the fuel. Empirical models are used to account for the pellet fragmentation, i.e., to estimate the fraction of the pellet surface in contact with the cladding.³⁴ In some particular scenarios, when the fuel centerline temperature exceeds 1200°C, significant cesium and/or molybdenum diffusion can occur toward the gap, leading to formation of [U, O, Pu, Cs, Mo, Zr] compounds in the gap. These compounds are viscous above 400°C.³⁵ Formed only when the gap is firmly closed, they are usually neglected in the gap conductance calculation.

The heat transfer in the fuel pellet: The heat transfer along the fuel pellet radius is usually evaluated without considering any impact of circumferential cracking. It can be justified by the slight temperature drop introduced by cracking, compared to the relatively large uncertainty in the fuel local power (often more than 10%). However, in one particular experiment (project High Burnup Chemistry) involving annular pellets, the multiplication of such cracks due to a grain separation at the annulus surface led to a quick gas release, and hence, to a 500°C increase of the centerline temperature at constant power.³⁶

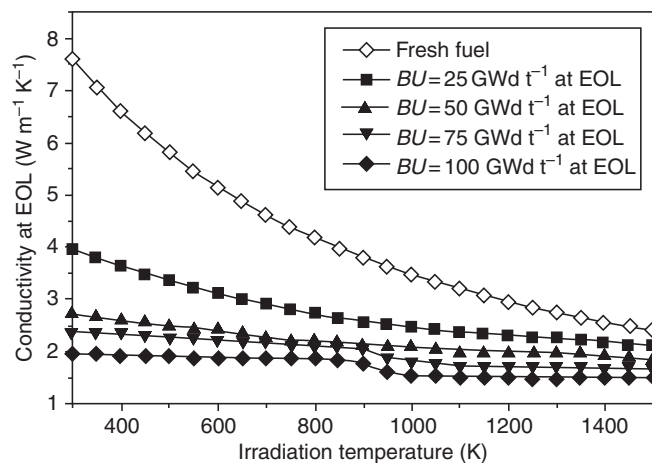


Fig. 16 Evolution of the intrinsic UO_2 fuel thermal conductivity with burnup.

- There are two components of the ceramic's conductivity: a phonon component dominant up to 2000K, decreasing with temperature, and an electronic component increasing with temperature and dominant above 2000K. The local fuel conductivity depends, in decreasing order, upon the temperature, local porosity (volume and shape mainly), the oxygen potential (oxygen defects), local burnup (fission products in solution, mainly number of point defects and density of dislocations), and probably weakly on plutonium content up to 25%.^{37,38} The fuel conductivity decreases with burnup as shown in Fig. 16. However, about 30% of this degradation is related to irradiation defects, which may be recovered during a local temperature increase.³⁹

The thermal conductivity of MOX, as measured on fresh fuel, is about 8% lower than for the equivalent UO_2 . However, for an average plutonium content not exceeding 15%, it has been demonstrated that the conductivity degradation is not related to the plutonium content as such, but rather to the modification of the local oxygen sublattice. Moreover, accounting for the degradation of the UO_2 fuel conductivity occurring as soon as irradiation begins, likewise due to perturbation of the oxygen sublattice, the initial MOX in-pile conductivity is effectively close to that of UO_2 . However, the heterogeneity of the MOX fuel leads to a differential degradation between the phases with burnup, which must be accounted for.

The evolution of the heat capacity of UO_2 was studied within the Nuclear Fuel Industry Research Group (NFIR III) project.⁴⁰ The main conclusion was that the heat capacity is not strongly influenced by the burnup as such. However, in the cold parts of the fuel pellets, the accumulation of irradiation defects may lead to an exothermic defect annealing in case of sudden temperature increase (observed in out-of-pile experiments). Nevertheless, based on experiments conducted by the UK Atomic Energy Agency within NFIR III, it was concluded that the observed phenomena will not have any measurable impact on in-reactor behavior. At this time, these conclusions are considered relevant for MOX fuel as well.

2.02.3.3 Mechanical Aspects

The mechanical performance is dominated by the interaction between the metallic cladding and (more or less) fragmented ceramic fuel pellets. Initially there is a gap between the two components, facilitating the introduction of the fuel pellets into the tube. As soon as irradiation starts, due to differential thermal expansions along their radius, the fuel pellets are fragmented, first in two pieces, then four, and so on,⁴¹ as power increases (Fig. 17). This fragmentation allows relaxation of the stresses induced by thermal expansion when the cracking limit is reached. The energy release tends to propel the fragments toward the cladding, a phenomenon called fragment relocation. The consequence is that the effective pellet-cladding gap is reduced. It is further reduced because of a higher thermal expansion of the pellet (fragments) than of the cladding, despite a higher thermal expansion coefficient of Zircaloy, because of the higher temperatures in the pellets. This higher thermal expansion of the pellets leads to a re-opening of the fuel-pellet gap, and of the cracks, when power decreases and particularly during shut-down periods. At beginning of life, the number of radial cracks range from 6 to 8 and 3 to 4 in the axial direction (Fig. 13). The second and third generation of cracks is obviously of more random type than the first generation.

Then, as irradiation proceeds, the fragments are forced toward the center by the cladding creep down. This creep is due to the coolant pressure (7–15.5 MPa, minus the internal gas pressure), and enhanced by the fast neutron irradiation. Progressively, after 1–3 years, with kinetics depending on many parameters (coolant pressure, initial gap, power history, fuel and cladding properties), a significant contact pressure begins to build between cladding and fuel pellet fragments. Because of the rough fragment surfaces, the relocation of the fragments, being pushed toward the center by cladding creep down, is reduced by their mutual interaction.⁴² The repetitive movement of the fragments with core power oscillations leads to a progressive wear of the fragment surfaces, which are then easier to relocate as shown in the French experiment 'RECOR'.⁴³ This period corresponds to a smooth, low-friction, pellet-cladding interaction.

Another aspect is the consequence of the steep radial temperature gradient in the fuel pellets, which leads to an 'hour-glass' shape of the pellets (Fig. 18). The consequence is a non-uniform gap closure along the pellet length, with a somewhat earlier

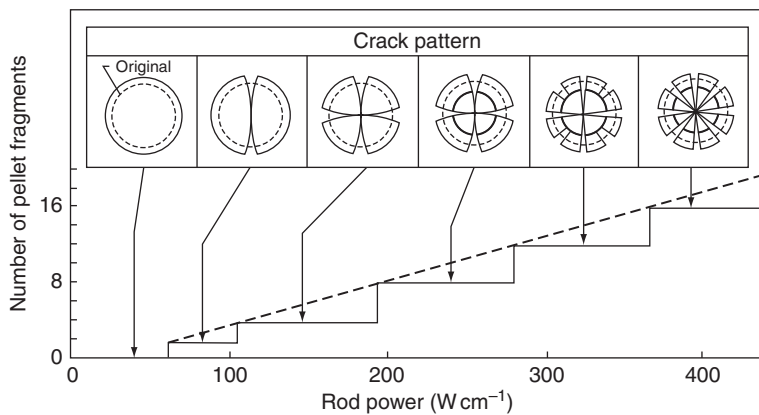


Fig. 17 Changes in crack pattern during rise to power. Reproduced from Oguma, M., 1983. Nucl. Eng. Des. 76, 35–45.

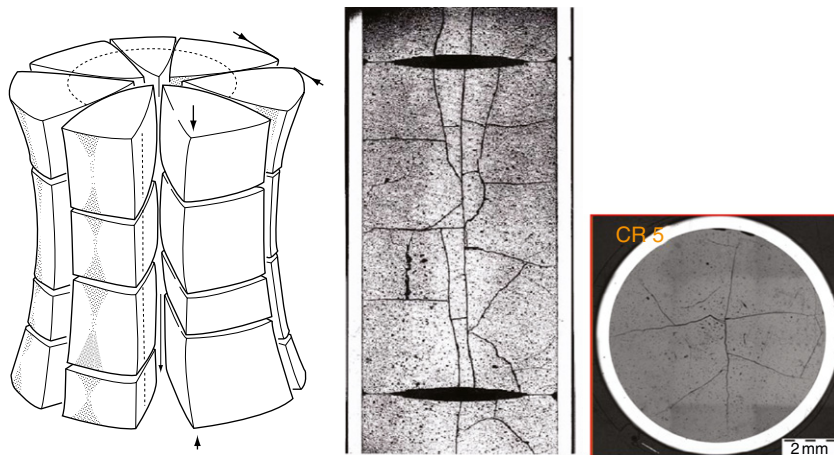


Fig. 18 Pellet hour-glassing (theoretical fragmentation).

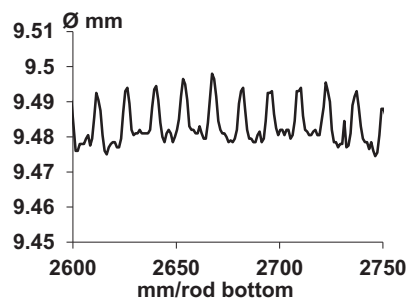


Fig. 19 Fuel rod cladding diameter profile after five annual irradiation cycles, showing primary pellet end ridges of about 15 μm (hour-glassing) and a beginning mid-pellet ridge. Courtesy of CEA.

closure near pellet ends. Therefore, pellet-cladding mechanical interaction starts near pellet-pellet interfaces, the exact location depending on the presence and geometry of chamfering, eventually leading to the "bamboo ridges" as observed on the cladding outer diameter axial profile (Fig. 19). The phenomenon is also called primary ridging. If total gap closure is not achieved, it can generate an axial rotation of the fragments (relocation). When hard contact is achieved all along the pellets, the maximum primary ridges range from 8 to 10 μm . The height obviously depends upon the pellet length, the fuel temperature gradient, chamfering, and end dishing of the pellets. During a power ramp, if local fuel temperatures are sufficiently high, gas swelling may also occur, inducing an additional deformation of the pellet. This can be observed on spent fuel rods by the formation of secondary ridges at mid-pellet locations, sometimes actually more pronounced than the primary ridges at pellet ends.

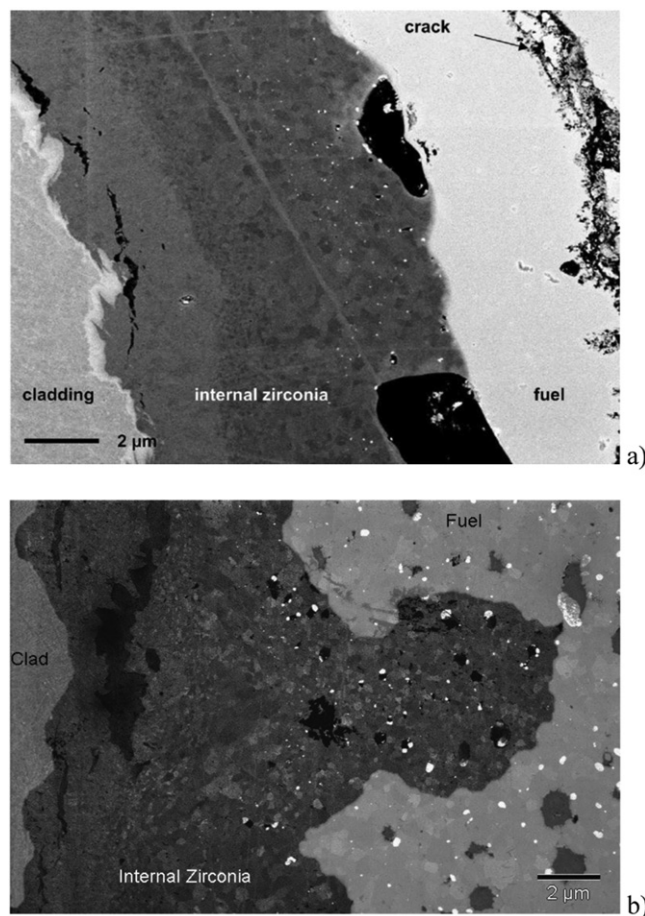


Fig. 20 SEM images of the zirconia layer formed on the cladding inner surface after (a) three annual cycles and (b) five annual cycles of irradiation, with a wavy interface. Reproduced from Ciszak, C., Desgranges, L., Garcia, P., *et al.*, 2019. J. Nucl. Mater. 520, 110–120. Ciszak, C., Mermoux, M., Miro, S., *et al.*, 2017. J. Nucl. Mater. 495, 392–404.

The fuel material is a porous ceramic obtained by powder pressing followed by sintering at high temperature (generally in the range 1700–1800°C). During irradiation, the fuel temperature is usually too low to activate additional thermal sintering. On the other hand, athermal sintering activation is possible. As addressed in Section 2.02.3.1 a large number of atoms are displaced for each fission event. This energy is sufficient to eliminate part of the remaining small porosity by re-implantation of vacancies from the pores to the bulk, and eventual annihilation on sinks, e.g., grain boundaries. This leads to an in-pile sintering of the fissile material, called “densification”.³ Densification follows a logarithmic evolution with time. Simultaneously, the fuel material swells due to several phenomena: the accumulation of non-soluble species, the accumulation of single or complex defects, the creation of new cells in the lattice, and the formation of precipitates. The combination of densification and swelling phenomena results in an increase of the density near beginning of life, followed by swelling of the material. The maximum density and the kinetics depend upon the fuel powder used (e.g., spherical or non-spherical grains) and the manufacturing techniques (e.g., pressure for compaction, use of pore former). In LWR fuel, the volumetric swelling rate is typically about 0.67% per at.% burnup. For higher temperatures (>1200°C, typically in power transient conditions), an additional swelling component is driven by the gas bubbles coalescence and vacancy trapping by these bubbles. This is the gas swelling mechanism, and we will see later in this article how gas swelling can be observed at high burnup. Once again, in MOX fuel, all the phenomena described here are induced in a heterogeneous manner, due to the multiphase character of the fuel material.

During irradiation, the combination of cladding creep down and fuel swelling leads to a progressive contact, until the pellets are in hard contact with the cladding. At this stage, the cladding creep is reversed, i.e., an outward creep is driven by pellet swelling. When a significant contact pressure has been established, interpenetration of species, mainly oxygen, may occur. In post irradiation examinations, one can detect the formation of zirconium oxide spots at the gap interface, at positions where hard contact was established during operation (Fig. 20).^{139,140} With the propagation of such hard contact to the entire interface, the zirconium oxide layer also propagates, and the species implantation as well, creating an effective chemical and mechanical bonding between the two materials. If the power then decreases suddenly, the gap is no longer able to reopen between the cladding and the fuel. This induces cracks within the fuel pellet periphery. Hence, the reopening of the gap is indeed within the pellet itself.

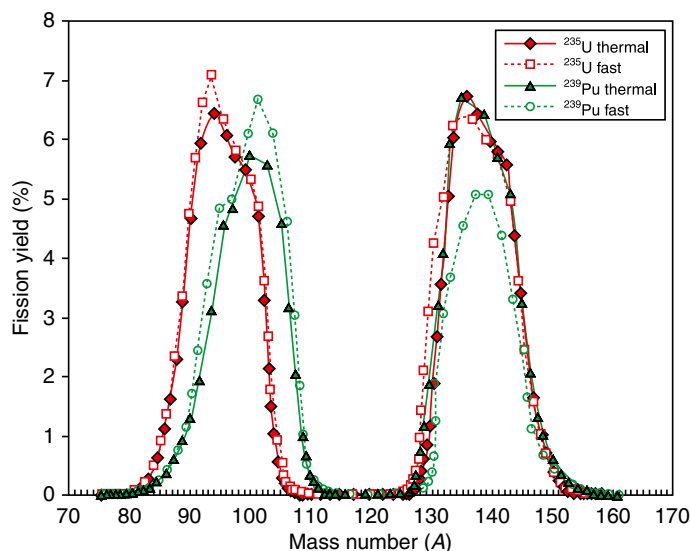


Fig. 21 Fission yields for ^{235}U and ^{239}Pu .

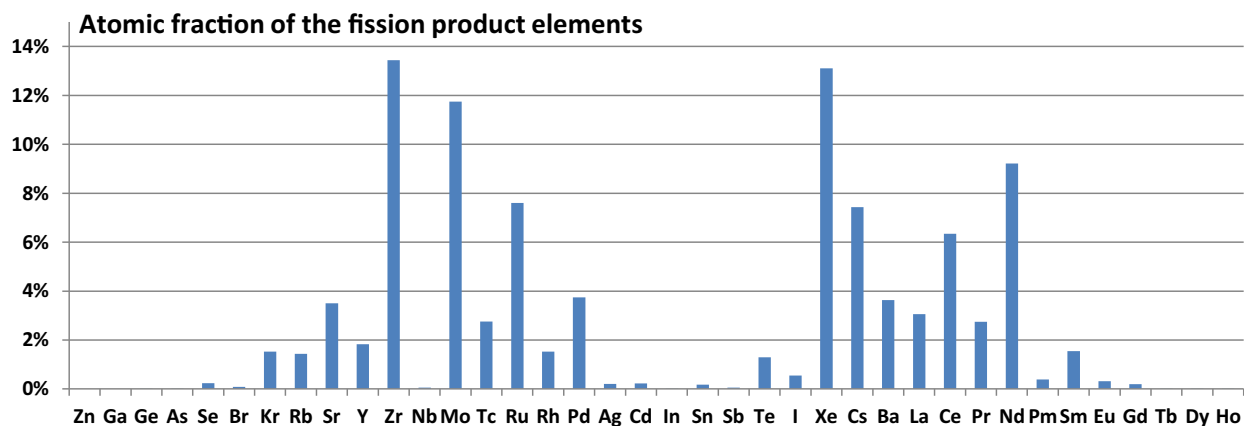


Fig. 22 Distribution of the atomic fractions of the fission product elements for a 4.49% ^{235}U UO_2 fuel at 40 MWd kgM^{-1} . Reproduced from Vidal, J.-M., Eschbach, R., Launay, A., et al., 2012. CESAR-5.3: An industrial tool for nuclear fuel and waste characterization with associated qualification. In: Proceedings of the Waste Management Symposia. Courtesy of CEA.

On the other hand, when the initial gap has not been entirely closed, there is a combination of bonded spots and free sliding at the interface, with friction conditions in intermediate location. This has no effect during normal operation, but can induce strong shear stress on the cladding in case of a transient. Moreover, the presence of zirconium oxide spots can have a negative effect regarding the risk to failure: Cracks in the (ceramic, brittle) oxide layer may act as incipient for defects in the metallic cladding wall.

2.02.3.4 Material Microstructure and Chemistry

The temperature of a fuel pellet in normal operation is within a range of 500–1200°C. These temperatures are not high enough to initiate any grain growth. On the other hand, during transients, temperatures can reach 2000°C at the pellet center. The grain growth mechanism then activated leads to equiaxial growth.⁴⁴ As opposed to the situation for FBR fuel, most LWR operational scenarios, will not activate columnar grain growth and the eventual formation of a central hole.

A great variety of fission products are generated. Fission yields for each species are specific to the respective fissile isotope: ^{235}U or ^{239}Pu mainly. Fig. 21 shows that the yield distribution is “camel back shaped” with two maxima. However, many of the generated species are unstable with short or very short decay periods, and some isotopes also have high capture cross sections and therefore will not accumulate in the fuel (Fig. 22).

A fission event typically leads to the appearance of two fragments in a mass ratio about 1/3–2/3. The dominant fission products are zirconium, xenon, molybdenum, neodymium, ruthenium, cesium and cerium, each with a yield greater than 6%. 19 species exceed 1 at%. The yields of these species are somewhat different between ^{235}U and ^{239}Pu , with a higher production of xenon for ^{239}Pu .

H																			He																																					
Li	Be											B	C	N	O	F	Ne																																							
Na	Mg											Al	Si	P	S	Cl	Ar																																							
K	Ca	Sc	Ti	V	Cr	Mn	Fe	Co	Ni	Cu	Zn	Ga	Ge	As	Se	Br	Kr																																							
Rb	Sr	Y	Zr	Nb	Mo	Tc	Ru	Rh	Pd	Ag	Cd	In	Sn	Sb	Te	I	Xe																																							
Cs	Ba	La	Hf	Ta	W	Re	Os	Ir	Pt	Au	Hg	Tl	Pb	Bi	Po	At	Rn																																							
Fr	Ra	Ac	Rf	Db	Sg	Bh	Hs	Mt	Ds	Rg	Cn	Nh	Fl	Mc	Lv	Ts	Og																																							
<table border="1" style="width: 100%; border-collapse: collapse;"> <tr> <td>Ce</td><td>Pr</td><td>Nd</td><td>Pm</td><td>Sm</td><td>Eu</td><td>Gd</td><td>Tb</td><td>Dy</td><td>Ho</td><td>Er</td><td>Tm</td><td>Yb</td><td>Lu</td><td></td><td></td><td></td><td></td><td></td></tr> <tr> <td>Th</td><td>Pa</td><td>U</td><td>Np</td><td>Pu</td><td>Am</td><td>Cm</td><td>Bk</td><td>Cf</td><td>Es</td><td>Fm</td><td>Md</td><td>No</td><td>Lr</td><td></td><td></td><td></td><td></td><td></td></tr> </table>																			Ce	Pr	Nd	Pm	Sm	Eu	Gd	Tb	Dy	Ho	Er	Tm	Yb	Lu						Th	Pa	U	Np	Pu	Am	Cm	Bk	Cf	Es	Fm	Md	No	Lr					
Ce	Pr	Nd	Pm	Sm	Eu	Gd	Tb	Dy	Ho	Er	Tm	Yb	Lu																																											
Th	Pa	U	Np	Pu	Am	Cm	Bk	Cf	Es	Fm	Md	No	Lr																																											
Oxides dissolved in the fuel					Gaseous or volatile																																																			
Metallic precipitates (alloys)					Ceramic precipitates (oxides)																																																			

Fig. 23 Chemical state of fission products in light water reactor fuel.

The final states of the fission products, after slowing down by ionization followed by collision cascades, depend upon their respective chemical affinities and sizes. In terms of experimental localization, an EPMA microanalysis involves a volume of approximately $1 \mu\text{m}^3$. This widely used post irradiation examination technique gives no indication of a possible heterogeneity at a lower scale. Moreover, depending on the lifetime of each isotope, some local and temporary association of unstable and stable species is likely to happen, but cannot be evidenced in the post-irradiation analyses.

The fission products can roughly be divided into four groups,⁴⁵ however, with a variability depending upon the local temperature and partial oxygen pressure:

- The fission products in solution in UO_2 , meaning that they are located in the UO_2 lattice, replacing a uranium or plutonium atom. These include Rb, Sr, Y, Zr, Nb, Cs, Ba, La, Ce, Pr, Nd, Pm, Sm, Eu, Gd, Tb, Dy, and Ho.
- The fission products able to form oxide precipitates, such as Rb, Sr, Zr, Nb, Mo, Cs, Te and Ba.
- The fission products forming metallic precipitates, such as Mo, Tc, Ru, Rh, Pd, Ag, Cd, In, Sn, Sb and Te.
- And finally, the gaseous and volatile fission products, able to diffuse and precipitate in bubbles when the local temperature exceeds their respective threshold diffusion energy, e.g., Xe, Kr, Br, Cs and I.

Fig. 23 summarizes these chemical affinities in the Mendeleev table. Obviously, this description is simplified and the reality is a bit more complex since various fission products are able to react with each other to form compounds, depending upon their chemical equilibrium diagrams versus temperature. Some of these compounds, such as CsI , can be volatile. Others such as Cs_2UO_4 are stable up to 800°C and viscous above 400°C .³⁵ Cesium and molybdenum are mobile in a temperature gradient when the local temperature exceeds 1200°C . In that case, these species generally migrate towards the pellet periphery and the pellet-pellet gaps. Ignoring the athermal atom movements due to fissions and collisions, neodymium is found to be quite stable in LWR fuels. It is therefore often used as a local burnup marker, reflecting the local proportion of ^{235}U and ^{239}Pu fission.

2.02.4 Consequences of Burnup Accumulation

2.02.4.1 Burnup

There are two primary perspectives on burnup. For core physics, burnup is the fraction of initial heavy metal atoms having been fissioned, given as an atomic percentage. In the industry, burnup is expressed as energy produced per unit heavy metal, e.g., megawatt-days per kilogram of initial heavy metal (MWd kgM^{-1}). A simplified relationship between these two burnup measures is

as follows:

$$BU(\text{at}\%) = 0.8955 \frac{(1 - \gamma) (eM_{235\text{U}} + (1 - e) M_{238\text{U}}) + \gamma M_{239\text{Pu}}}{E_{\text{fiss}}} \times BU(\text{GWd/t}_M) \quad (6)$$

where $M_{235\text{U}}$ is molar mass of ^{235}U (g), $M_{238\text{U}}$ is molar mass of ^{238}U (g), e is the ^{235}U enrichment, $M_{239\text{Pu}}$ is molar mass of plutonium (g), γ is the Pu/(U + Pu) fraction, and E_{fiss} is the average fission energy (MeV).

The application for UO_2 is roughly:

$$BU(\text{at}\%) = 0.10884 \times BU(\text{GWd/t}_M) \quad (7)$$

As the burnup proceeds, the fuel is subject to a chemical and physical transformation, due to several processes:

- Progressive transmutation of the fissile atoms and accumulation of fission products, including the appearance of new fissile atoms (plutonium) generated from neutron absorption by ^{238}U in the epithermal energy domain.
- The accumulation of irradiation point defects and dislocation loops. Their thermal recovery is limited, in particular in the cold regions of the pellet. A partial athermal recovery is activated by fission energy. The number density of dislocations gradually increases, up to about 45 MWd kgM^{-1} , after which the dislocation loops are progressively entangled.²⁸ This leads to an increase of the lattice parameter.²⁷
- An evolution of the local oxygen potential, which increases moderately.⁴⁶
- The accumulation of gaseous fission products, non-soluble in UO_2 . These tend to precipitate in bubbles, modifying local material porosity and contributing to fuel swelling.

To understand fuel material evolution, it should be realized that local changes are mainly related to (local) temperature, burnup and fission rate, fission recoil-induced movements of heavy atoms, oxygen, and also of the previously formed fission products. However, the crystal structure is maintained. Due to fission and transmutation, the material continuously evolves, increasingly differing from the initial fuel, with an average chemical composition that depends on radial location. Moreover, as soon as the fuel begins irradiation, the oxygen sublattice is modified. Since most of the physical properties are sensitive to oxygen sublattice defects, all these processes have to be accounted for in the evaluation of local properties.

For MOX fuels, due to the heterogeneity of the plutonium distribution, and therefore, power generation, one must account for the different phases in an assessment of material evolution:

- Plutonium-rich agglomerates
- UO_2 particles with low plutonium content
- Intermediate phases

The phases will have different fission densities, leading to a differential evolution of parameters: local burnup (as shown in Fig. 24), chemical composition, dislocation density, lattice parameter, gas, and metallic precipitates.

Implantation processes, driven by recoil, tend to somewhat reduce the difference between phases. The heterogeneity causes nonuniformity also in the fission product distribution, and therefore has an effect on the overall material properties. Moreover, the high burnup transformation (HBS, "rim structure") (Section 2.02.4.5) starts earlier in the plutonium agglomerates due to their higher burnup.

2.02.4.2 Behavior of the Gaseous and Volatile Fission Products

The fission gas release and fuel gaseous swelling mechanisms are extensively described by Olander.³ An International Atomic Energy Agency (IAEA) seminar focusing on this subject was held in Cadarache (France) in 2000.⁴⁷ Two reviews on this subject have also been recently published.^{48,49}

The behavior of gaseous and volatile fission products is one of the major concerns in LWR fuel design, since it affects the dimensional stability of the pellets as well as the evolution of rod inner pressure. Moreover, some volatile fission products such as cesium, iodine, and tellurium may react with the zirconium cladding, that is, contribute to a PCI failure. Xenon has the largest fission yield, for uranium as well as for plutonium, that is, about 13% of the overall fission generated atoms in UO_2 fuels and about 14.6% in MOX fuels. Krypton has a fission yield a decade lower than xenon. Both are considered nonsoluble in the fuel matrix and require a point defect to accommodate their large size, thereby inducing a local deformation of the lattice. In order to relax the internal energy, the trend for these gaseous fission products is to migrate and precipitate in traps such as bubbles and grain boundaries. The higher the temperature, the faster the diffusion. The bubble's behavior has not yet been fully understood. A fraction of the fission products precipitate in the fuel (solid and gaseous). These precipitates can act as initiation points for nano-bubble formation followed by growth, enabled by a flow of vacancies. Bubbles might also form in the fission spikes, where the energy of newly formed fission products is transferred to the crystal by electronic interaction. Bubbles act as traps for gaseous fission products, moving both by thermal diffusion and athermal processes (recoil when the atom is produced by a fission event, displacement through interaction with recoiling fission products, or in cascades induced by recoil). These athermal processes can also knock out gas atoms from inside a bubble, or even annihilate a tiny bubble. This is called the re-solution process.⁵⁰

At low temperature, athermal processes dominate, slowly and progressively filling grain boundaries with all kinds of fission products (not only gaseous) and leading to a low level gas release from the fuel by knockout and recoil processes occurring close to

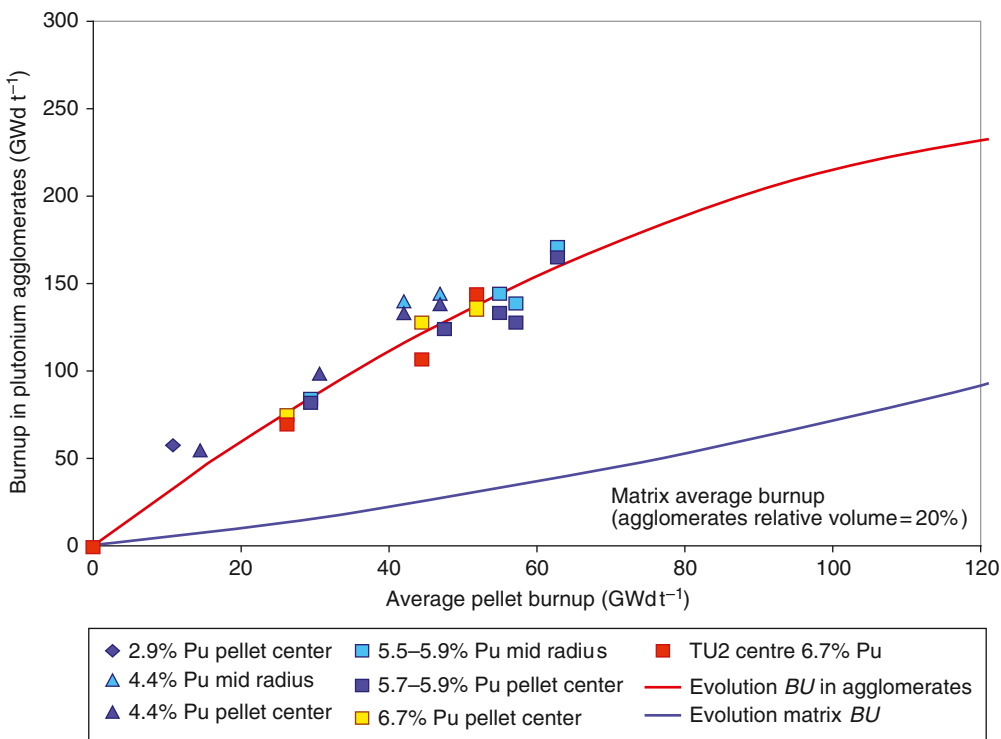


Fig. 24 Mixed oxides fuels – evolution of the phase burnup assuming two phases: agglomerates rich in plutonium spread in a UO_2 matrix.

free surfaces. This fission gas release level is strongly related to the amount of open porosity (i.e., ratio of free surface to volume). The instantaneous fission gas release fraction can be calculated by the following equation⁵¹:

$$\frac{R}{B} = \frac{1}{4} \frac{S_g}{V} \mu_f + \frac{S_t}{V} \cdot \frac{\mu_f \alpha_U \dot{F}}{4 \lambda N_U} \quad (8)$$

where $\frac{R}{B}$ is the instantaneous fission gas release: ratio release to birth, S_g geometrical surface of the fuel pellet (m^2), S_t developed fuel pellet surface (m^2), V pellet volume (m^3), μ_f average fission fragment free path (m), α_U number of fission fragments, N_U number of uranium atoms per volume unit (m^{-3}), \dot{F} instantaneous fission density (fission $\text{m}^{-3} \text{s}^{-1}$), and λ decay constant for the considered species.

Note that the first term represents the recoil phenomenon, independent of the decay constant λ , and the second term the knockout process, inversely dependent on the decay constant.

At higher temperatures (above 800°C), thermal diffusion starts to dominate. At intermediate temperatures, the major process is an atomic diffusion of gases. However, vacancies move faster than gas atoms, contributing to bubble formation and growth, both within grains and on grain boundaries. Bubbles are efficient traps for gas atoms, but grain boundaries are also efficient sinks, even if a small fraction can eventually return through the grain surface by knockout processes (a few micrometers deep into the grain).

Grain boundaries are efficient traps, not only for gases but also for solid fission products and vacancies. These elements mechanically weaken the grain boundaries and pin the bubbles. Tiny bubbles also appear and grow inside grains. Depending on irradiation condition, and particularly on local temperature, the growth of these bubbles can be restrained: Most of the bubbles remain separated from their neighbor bubbles, tunnels can form along grain edges (triple boundaries) or bubbles can interconnect, progressively building tunnel-like mazes, eventually opening to the edge of the fuel grains, thus forming paths for fission gas release.^{52–54} This can be seen in Fig. 25 (left SEM image on a smoothly polished surface) where bubbles are aligned mainly along the grain boundaries. The right picture in Fig. 25 is a SEM observation of a fractured surface showing a large bubble precipitating on the grain surface. In Fig. 25 (right picture) bubble coalescence is evidenced by the appearance of oblate bubbles on the grain surface. Fig. 26⁵⁵ shows an example in which the fuel was brought to a very high linear heat rate for a short period of time (see Section 2.02.5) and where grain boundaries exhibit metallic fission product precipitates (the almost spherical bright spots), isolated intergranular bubbles, interconnected intergranular bubbles and grain edge tunnels. However, in many high burnup fuels the actual release paths are not clearly visible. This will be discussed in Section 2.02.4.5. together with the case of the quasi micron sized bubbles formed at high burnup. The growth and coalescence of bubbles induces gaseous swelling of the material as long as the gases are not efficiently released.

In a simplified approach, the Fick equation can be used to describe gas diffusion within the grains. It includes five components corresponding to five separate phenomena:

- Gas isotope yield
- Atomic gas diffusion
- Isotope decay

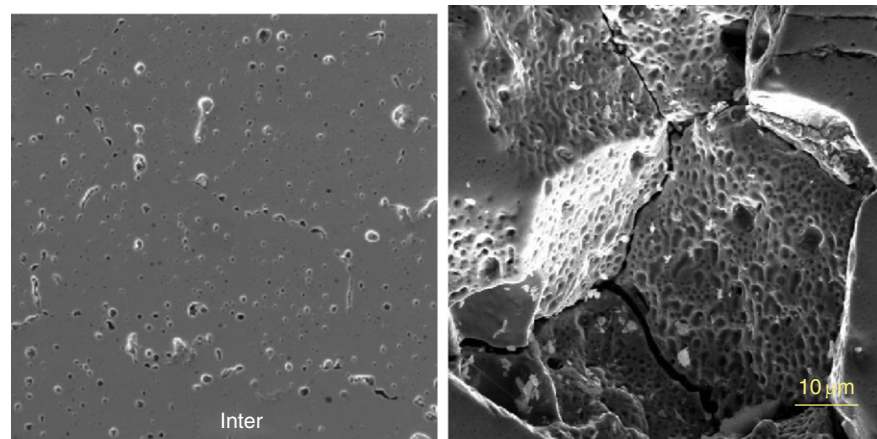


Fig. 25 Bubble formation and coalescence at grain boundaries.

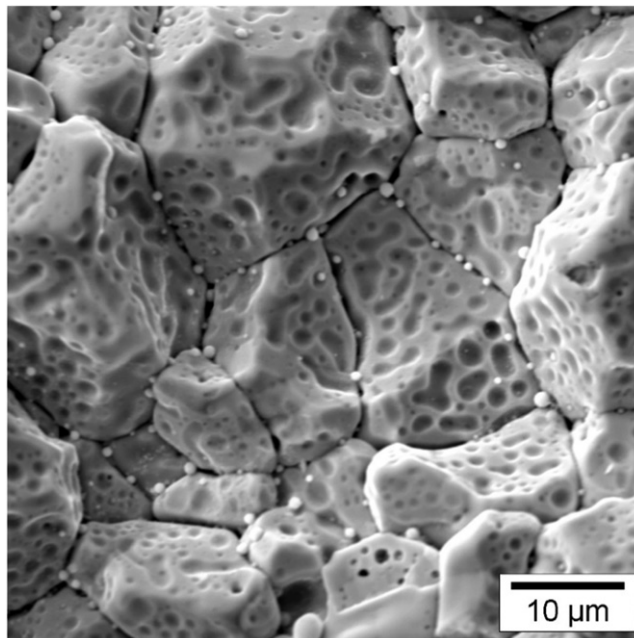


Fig. 26 SEM fractograph of the central part of a 39 MWd kgM⁻¹ UO₂ PWR fuel after a ramp test in the Osiris reactor, where the linear heat rate was kept at 520 W cm⁻¹ during 90 s. Reproduced from Noirot, J., Gonnier, C., Desgranges, L., et al., 2009. LWR Fuel Gas Characterization at CEA Cadarache LECA-STAR Hot Laboratory. IAEA-TECDOC-CD-1635.

- Gas trapping in bubbles
- Gas re-solution from bubbles

$$\frac{\partial C}{\partial t} = \dot{F} + \frac{1}{r^2} D \frac{\partial}{\partial r} r^2 \left(\frac{\partial C}{\partial r} \right) - \lambda C - \sum_j g_j C + \sum_j b_j M_j \quad (9)$$

where C is isotope concentration at time t and radius r (mol m⁻³), r radius in the grain (m), \dot{F} instantaneous fission density (fission m⁻³ s⁻¹), λ decay constant for the considered species (s), g_j trapping efficiency for type j trap, b_j resolution coefficient from type j trap, M_j gas concentration in type j trap (mol m⁻³), and D gas diffusion coefficient (m² s⁻¹).

The xenon diffusion coefficient in the fuel matrix under irradiation is usually described by three terms representing the thermal contribution, athermal mechanisms (recoil and knockout) and the influence of vacancies created under irradiation (mixed term)⁵⁶⁻⁵⁸ (Fig. 27):

$$D_{Xe} = D_{th} + D_{ath} + D_{mix} \quad (10)$$

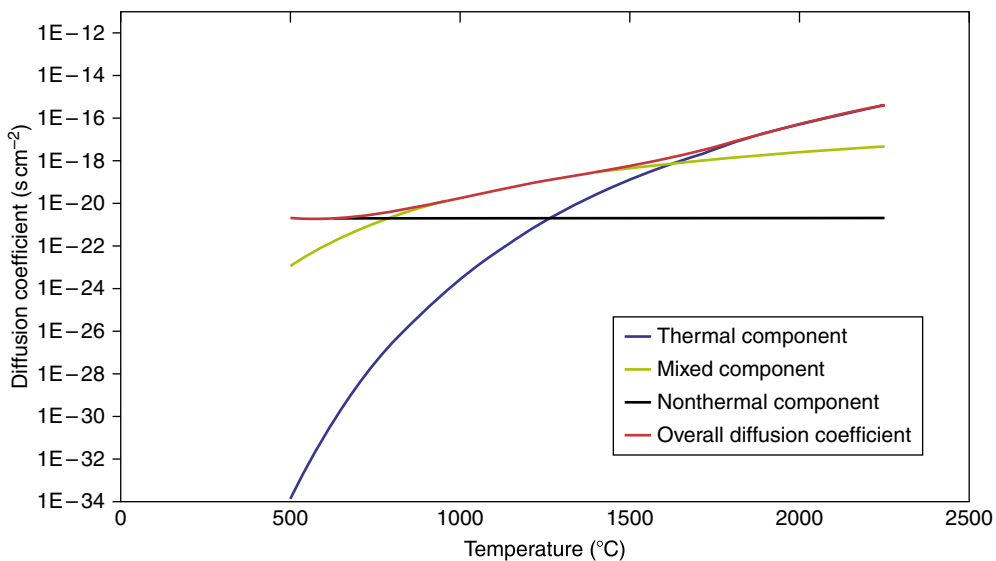


Fig. 27 Turnbull diffusion coefficient.

The thermal contribution is:

$$D_{th} = 7 \cdot 6 \cdot 10^{-10} \cdot \exp\left[-\frac{35225}{T}\right] \quad (11)$$

The pure athermal contribution is:

$$D_{ath} = 6 \cdot 10^{-40} \cdot \dot{F} \quad (12)$$

With a mixed term for vacancies:

$$D_{mix} = 1 \cdot 39 \cdot 10^{-24} \cdot \frac{\sqrt{\dot{F}}}{2} \exp\left[-\frac{13870}{T}\right] \quad (13)$$

In the simplified approaches, the gas behavior on grain boundaries is not directly described. The diffusion equation is solved in a theoretical sphere, the radius of which decreases with burnup, as grain boundaries progressively open due to gas and fission products accumulation.^{59,60} The minimum value is reached when it becomes equivalent to the local average grain size of the material. In steady-state conditions, the solution of the differential equation yields³:

$$f = \frac{3D}{\lambda a^2} \left[\left(\frac{\lambda a^2}{D} \right)^{\frac{1}{2}} \coth \left(\frac{\lambda a^2}{D} \right)^{\frac{1}{2}} - 1 \right] \quad (14)$$

where a is the radius of the Booth sphere (m) and f is the fraction of fission gases released.

Assuming $\left(\frac{\lambda a^2}{D}\right)^{\frac{1}{2}} \gg 1$, we get:

$$f = 3 \left(\frac{D}{\lambda a^2} \right)^{\frac{1}{2}} \quad (15)$$

Thus, the gas thermal diffusion is inversely proportional to $\lambda^{\frac{1}{2}}$.

More advanced models now exist, such as the MARGARET^{61,62} and CARACAS^{63,64} models by the CEA, attempting to assess in detail all the different processes within the grains and in grain boundaries, including atomic gas diffusion, bubble growth and coalescence in order to accurately simulate fuel swelling and fission gas release. Experimental characterization combining (mainly) SIMS analysis and EPMA are still being improved in order to validate these models in terms of gas repartitioning between matrix and bubbles, and between the inside of grains and grain boundaries. Attempts are also being made to experimentally evaluate the gas pressure in bubbles as a function of their size.

Fission gas release generally remains quite low during normal LWR operating conditions (see **Fig. 28**), as long as the centerline temperature does not exceed the Vitanza *et al.*⁶⁵ threshold. The 'Vitanza curve,' also called 'Halden threshold,' is an empirical curve originally used to monitor the Halden reactor irradiations. For a given fuel rod burnup, it yields the linear heat generation rate (kW m^{-1}) at which the fission gas release exceeds 1% of the gas generated. The thermally activated release is indeed a threshold mechanism. Beyond this threshold, fission gas release increases by about 3% per 100°C centerline temperature. The Vitanza curve is an empirical rule-of-thumb for burnups ranging from 0 to 60 MWd kgM^{-1} , as long as fuel restructuring (HBS formation) remains small, and fuel fragmentation is also limited.

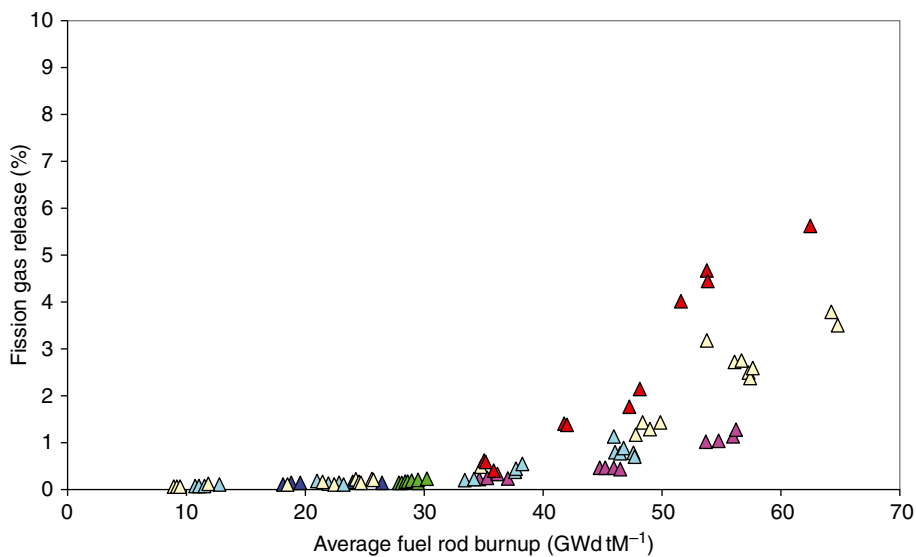


Fig. 28 Fission gas release in UO_2 -pressurized water reactor fuel rods during normal operating conditions.

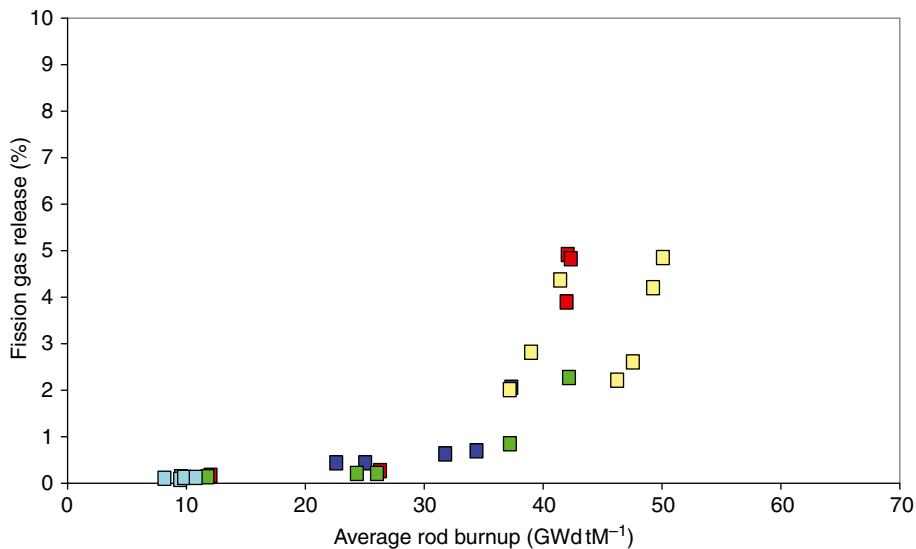


Fig. 29 Fission gas release in mixed-oxides-fuel-pressurized water reactor fuel rods during normal operating conditions.

Even if gases are not released, they progressively accumulate in grain boundaries as burnup proceeds, weakening them. They are directly available for release in case of grain boundary separation, e.g., during RIA transients. Such grain separation is caused by sudden power variations inducing large local micrometric stress fields.

Thermally speaking, in UO_2 fuels the centerline temperature is usually close to, or slightly above, the temperature for which thermal diffusion becomes significant, in particular during the first two years of operation.

Obviously, the fission gas release fraction in an LWR fuel rod can attain much higher values in case of accidents, e.g., up to 50% at power levels around 500 W cm^{-1} . Such power levels are, however, not attainable at high burnup because of the reactivity decrease.^{9,10}

MOX fuels generally exhibit a higher fission gas release at normal operating conditions and during accidents, due to the fact that their reactivity is still relatively high at high burnup (Fig. 29).

However, the heterogeneity slows down the average fuel conductivity degradation and therefore also the release rate growth with burnup. The HBS structure in the agglomerates and the specific behavior of such restructured material leads to a higher sensitivity to the temperature of the MOX fuel, compared to UO_2 . The restructured phases tend to release 80% of their accumulated gas as soon as the local temperature passes beyond a threshold temperature, evaluated from Knudsen cell experiments to be in a range of $1100\text{--}1300^\circ\text{C}$.^{66,67} In UO_2 fuel, the HBS rim region never reaches such temperatures during normal or accident conditions. This is obviously true also for the MOX rim region. On the other hand, the restructured MOX agglomerates located in

the central parts of the pellet can be affected. This is the reason for the sensitivity of MOX fuel to temperature, with respect to fission gas release.

In UO_2 fuels, helium production during irradiation is sufficiently small to be neglected. For MOX fuel, however, due to the high α -particle generation, helium is a significant contributor to the evolution of gas pressure in the free volumes. During irradiation, a large number of heavy isotopes are formed from neutron capture or fission, and their decays generate one or several α -particles. Due to the presence of such higher isotopes in fresh MOX fuels (plutonium 239, 240, 241, 242, americium, and curium), these fuels exhibit a significant α -emission even before irradiation begins and after irradiation (see Section 2.02.2.2.1). In fact, there are three significant modes of helium production:

- 68% is due to α -decay of heavy actinides (^{238}Pu for 4%, ^{244}Cm for 21%, ^{242}Cm for 75%)
- 25% is generated by (n, α) reactions of ^{16}O
- 7% is due to ternary fissions (fission directly combined with an α -decay)

The helium behavior in fuel during irradiation is very different from that of xenon or krypton due to the very small size: helium does not interact strongly with the fuel lattice and can therefore easily migrate in the fuel material, interacting with existing pores and bubbles, grain boundaries, and the free volume. There is obviously no difference in behavior between helium generated during irradiation and the helium initially introduced as fill gas. During a transient, helium is released faster than the heavy noble gases. Hence, specific modeling of helium behavior is required for the simulation of MOX fuels.

2.02.4.3 Evolution of the Oxygen Potential

Uranium or plutonium fission generates fission fragments and releases two oxygen atoms. Most of these oxygen atoms are able to recombine with the fission products when they stabilize in the fuel matrix. This is obviously not the case for the noble gases (about 15% of the fission products), nor for the noble metals, forming alloy precipitates. In the operating temperature range, fission products can be mono-, bi-, tri-, or quadrivalent. Moreover, more complex oxides can be formed with molybdenum, barium, cesium, etc. Fig. 30 shows the equilibrium oxygen potentials for different metal/metal-oxide mixtures.⁴⁶

This leads to a quite slow, global increase of the oxygen potential as burnup proceeds.^{46,68,69} The oxygen potential ($\Delta G(\text{O}_2)$) data for LWR fuel is generally measured by the EMF method. The data analyzed by Spino *et al.* shows that at a burnup higher than 80 MWd kgM^{-1} , up to 100 MWd kgM^{-1} , the UO_2 fuel tends to become slightly hyperstoichiometric (Fig. 31). The maximum O/M ratios potentially achieved at 100 MWd kgM^{-1} would range only between 2.001 and 2.002, accounting for an initial O/M in fabrication between 2.000 and 2.005. The limited deviation from stoichiometry is attributed to the oxygen uptake by the cladding (inner wall, generating ZrO_2) and possibly a partial oxidation of Mo. Notably, all measurements are performed post-irradiation, in a hot-cell laboratory. To this day, there is no experimental method to determine oxygen potential during irradiation. These conclusions are obviously very dependent upon the power history of the LWR fuel.

In MOX fuels where the burnup in the Pu-rich agglomerates can be higher than in the UO_2 HBS rim, a partial lack of molybdenum from the HBS peripheral precipitates is often measured together with an increase of the molybdenum content in the rest of the Pu-rich agglomerate.⁷⁰

2.02.4.4 Evolution of the Properties

Most of the physical properties of the fuel change as irradiation proceeds. This is mainly due to the modification of the oxygen sublattice, the lattice defect accumulation, and the incorporation of fission products. When burnup increases, despite the high mobility of atoms by collision cascades, the fuel matrix accumulates lots of defects, which can evolve more or less depending upon the local temperature. The fuel porosity also evolves locally by densification (resintering processes) or gas precipitation. Due to metallic and ceramic precipitations, the material becomes a multiphase system. Moreover, the grain boundaries are drastically modified with the accumulation of gasses and fission products, potentially forming bubbles and precipitates. All these factors lead to a gradual global modification of the physical and mechanical properties of the fuel material. Concerning fuel mechanical properties, a lot of data have been acquired for fresh fuel. Compressive tests or three-point bending tests have enabled the development of thermal creep models. Failure properties have likewise been obtained for modeling, by conducting such tests. However, mechanical data (elastic properties and failure properties), and kinetics (e.g., thermal creep laws) are much more difficult to measure for the cracked pellets of irradiated fuel. Measurements of failure properties and creep behavior of irradiated fuel have been performed, or are proposed, by several organizations.^{71–74} With regard to elastic properties, micro-hardness tests have been performed since 1994, mainly by JRC Karlsruhe.⁷¹ Techniques are also proposed in the JRC hot laboratories in collaboration with EDF R&D to assess these properties⁷²: focused acoustics operating at 230 MHz for the local elastic properties at room temperature and micro-indentation in controlled atmosphere, from room temperature up to 1200°C.

The fuel density evolves by densification and solid swelling together with gaseous swelling. Fig. 32 shows a gradual decrease of the density with burnup. In LWR operation, density typically decreases, following roughly the solid swelling rate, up to 55 MWd kgM^{-1} , and then accelerates due to gaseous swelling (growth of gas bubbles, mainly in the rim region and at the pellet center).

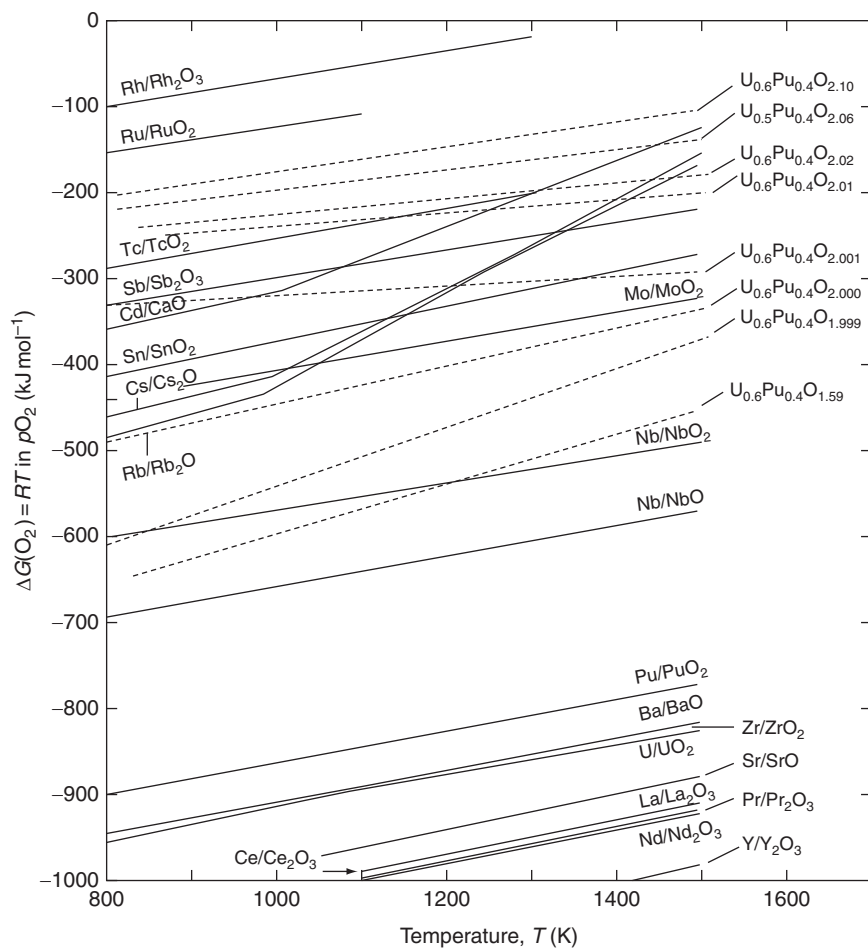


Fig. 30 Free energy formation of the main fission products oxides compared to $U_{0.6}\text{Pu}_{0.4}\text{O}_{2\pm x}$ for various x values. $U_{0.6}\text{Pu}_{0.4}\text{O}_{2\pm x}$ phase is here considered representative of the fuel state at high burnups. It shows that Cs, Rb, and Mo oxidation depends upon the fuel oxygen potential. Reproduced from Spino, J., Peerani, P., 2008. J. Nucl. Mater. 375, 8–25.

2.02.4.5 Grain Restructuring

2.02.4.5.1 HBS grain restructuring at the UO_2 fuel periphery and in MOX Pu-rich zones

When thermal recovery is not sufficiently efficient, the accumulation of defects at high burnup can lead to instability of the crystalline structure, initiating a restructuring driven by the energy stored in the material. In the cold regions of the fuel, operating at temperatures lower than 800–900°C, no significant thermal diffusion should usually be expected. However, an athermal phenomenon was demonstrated in the 1980s in the first LWR high burnup fuels.⁷⁵ It was then widely studied during the next 20 years. To be correct, it must be mentioned that early observations had already been reported by Barney *et al.*⁷⁶ in 1958 and by Bleiberg *et al.*⁷⁷ in 1963.

A low temperature transformation is observed beyond a local burnup of around 55–60 MWd kgM⁻¹, leading to the appearance of a micron sized and dense porosity, accompanied by grain subdivision (Fig. 33), with typical grain sizes ranging from 200 to 500 nm. This phenomenon was first called ‘rim effect’, since in the UO_2 fuel pellets it starts at the high burnup periphery.

A large number of publications are focused on the analysis of the phenomenon,^{14,27,46,70,78–81} or a multiscale approach.⁸² As a complement to the various national survey programs, HBS was investigated in several international parametric experimental studies, in particular the following projects: High Burnup Effect Program (HBEP),¹⁰ High Burnup Rim Project (HBRP),^{14,83–85} HBRP_NT,¹⁵ and some new projects such as New Cross over Project (NKO)⁸² and F-Bridge.⁸⁶ Simplifying, the HBS transformation can be described as follows:

- Increasing defect density in the crystal and formation of an entangled dislocation network.²⁸
- These dislocations organize at a sub-micrometric scale, piling-up to form “walls”. Local crystal orientations differ slightly from the orientation of the original grain.
- This leads to the formation of sub-grains, with orientations remaining close to that of the original grain. Fission gases accumulate in 10–100-nm-sized bubbles on sub-grain boundaries. Nanometric bubbles are still observed inside sub-grains.
- Among the slightly misoriented sub-grains, formation of new grains with high boundary angles. This process is likely to be a recrystallization. As a consequence, gas is swept out of the crystal and feed the fission gas bubbles, according to Ref. 87, through

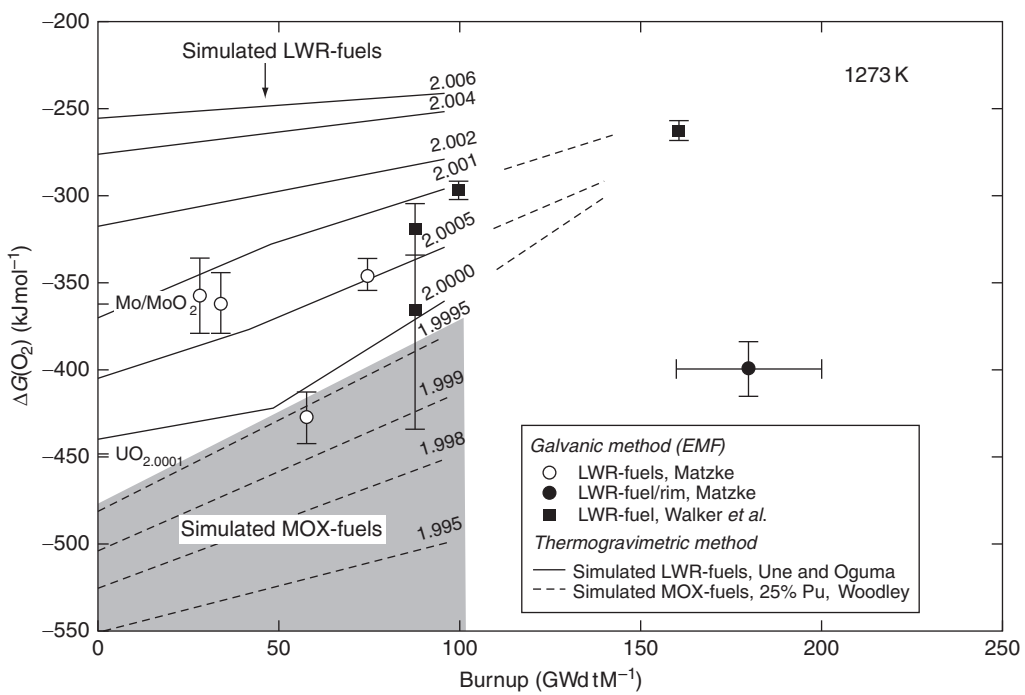


Fig. 31 Compilation of oxygen potential vs. burnup. The oxygen potential found for irradiated fuel is consistent with nearly stoichiometric simulated LWR and MOX fuels. Reproduced from Spino, J., Peerani, P., 2008. J. Nucl. Mater. 375, 8–25.

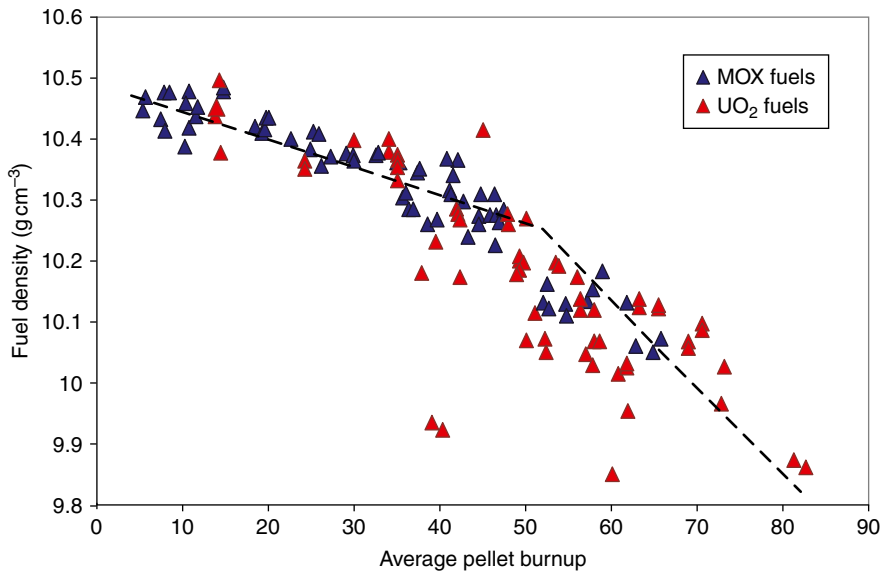


Fig. 32 Evolution of the average fuel density with burnup.

interconnected nanobubbles on the boundaries of these grains. Intergranular metallic fission product precipitates are also observed. The gas remaining in the grains decreases and Xe reaches concentrations close to 0.1 wt%, while its production is higher than 1.5%, (Fig. 34 and Ref. 70).¹⁴¹

- The high angle orientation sub-grain formation spreads and more or less covers the whole local volume, (Fig. 34).
- With ongoing irradiation, there is a continuous growth of the intergranular bubbles, fed by vacancies and by newly generated gases, also by bubble coalescence and possibly by Oswald ripening⁸⁸ (but if so, that would mean that gas trapped in bubbles can be re-dissolved in the grains, or at the new grain boundaries, and can eventually diffuse to larger bubbles. This is, however, not clearly established). Consequently the bubble number density decreases.

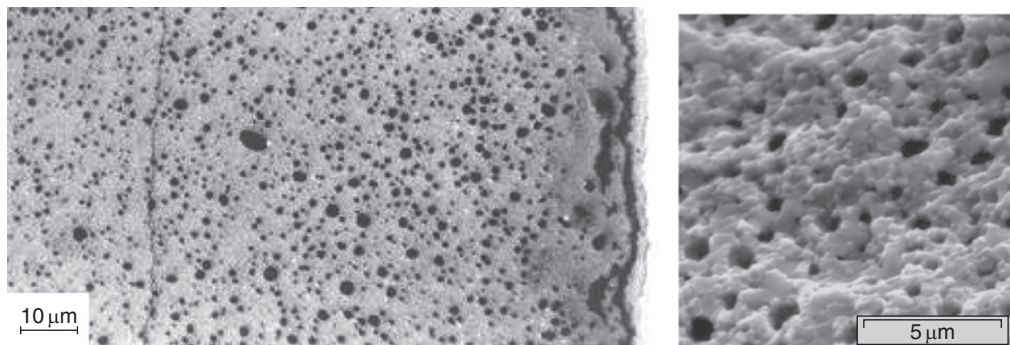


Fig. 33 High burnup structure transformation with the apparition of a micron sized and dense porosity, accompanied by a grain subdivision.

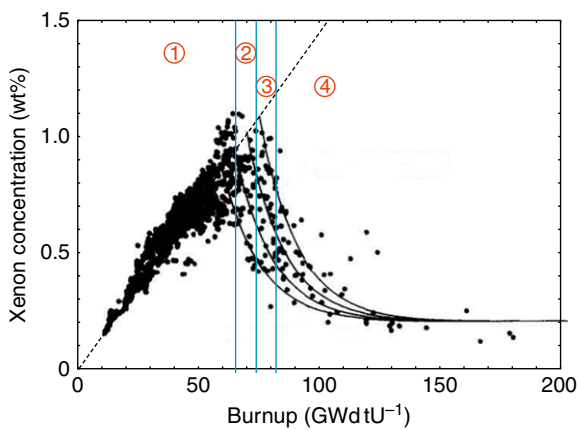


Fig. 34 Electron probe microanalysis xenon detection vs. local burnup in pressurized water reactor UO_2 fuel pellets. Reproduced from Lassmann, K., Walker, C.T., van de Laar, J., Lindström, F., *et al.*, 1995. J. Nucl. Mater. 226, 1–8.

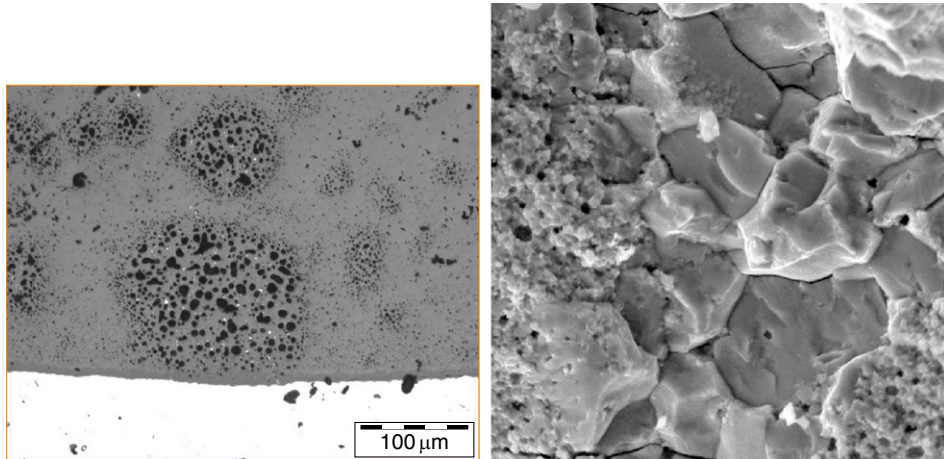


Fig. 35 Mixed oxides fuels – high burnup structure restructuring firstly in the plutonium-rich agglomerates optical image on the left and MEB fractograph on the right.

- At very high burnup, or in high burnup MOX Pu-rich agglomerates, this evolution is such that⁸⁹ proposed the notion of ultra-high burnup structure (UHBS).

It was demonstrated from various approaches, particularly with EPMA and SIMS joint analysis, that gases remain trapped in the HBS bubbles and that the increasing rate of fission gas release observed at high burnup is not directly due to HBS formation^{80,90–93}

In MOX fuel, the HBS transformation begins already during the second year of irradiation, due to the higher burnup in the Pu-rich agglomerates, as shown in **Fig. 35**. The Pu-rich agglomerates exhibit HBS with a high micron-sized porosity when the rest of the material

is still not restructured. The HBS transformation can occur deep within the pellet, toward the mid-radius, depending on the radial temperature profile during irradiation. For higher MOX pellet (average) burnups, all phases are affected by restructuring in the pellet rim, analogously to UO₂ fuel. Examination of MOX fuels and of sodium cooled fast reactor fuels, in which HBS formation is also observed, show that at a given local burnup, the bubbles and sub-grains are larger for higher irradiation temperatures.^{21,70,94,95} Even though most of the gas is retained in the bubbles during HBS formation, and MOX Pu-rich agglomerates make no exception, examinations have shown cracked HBS agglomerates having released most of their bubble's gases.⁹⁶

The HBS structure also exhibits a very particular behavior leading to fuel fragmentation and fission gas release in case of LOCA (loss of coolant accidents) scenario, when local temperatures exceed ~800°C and, simultaneously, compressive stresses are reduced, e.g., due to a temperature-driven softening of the Zr cladding and to core pressure decrease.^{67,97–105}

The presence of restructured agglomerates deep within the pellet causes a susceptibility of MOX fuel to an enhanced thermal fission gas release during transients and LOCA scenarios.¹⁰⁶

Several models were developed to simulate HBS transformation,^{62,107–117} some of which are briefly described in Ref. 118. The modeling is obviously still improving,¹¹⁹ following the evolution of our understanding of the underlying mechanisms at the atomic scale.

Naturally, all this material restructuring has a strong effect on material properties and structural interactions. The increase of the relative porosity volume degrades the material conductivity but increases viscosity and reduces the mean grain size. On the other hand, the intragranular sweeping of irradiation defects and fission products improves the intrinsic thermal conductivity.¹²⁰ The presence of viscous phases on grain boundaries can be expected, which also improves the overall viscosity in a pellet-cladding interaction scenario. All these aspects are understood to explain the demonstrated good behavior of high burnup fuel regarding PCI/PCMI in power ramps. The HBS behavior in LOCA situations is also the focus of modeling work.^{121,122}

2.02.4.5.2 UO₂ fuel central area grain restructuring

Most of the rods reaching a high discharge burnup experience decreasing linear heat rates in their final cycles (Figs. 8 and 12). Despite the gradual thermal conductivity decrease of the fuel, this linear heat rate reduction leads to a gradual decrease of the central fuel centerline temperatures. Nevertheless, as seen in Fig. 28, fission gas release fractions typically increase with burnup. In the same burnup range as the onset of HBS rim formation, a high sub-micron-sized intragranular and intergranular bubble formation is observed in the center region of UO₂ fuels, even in the case of low final linear heat rates. (Fig. 36).^{92,119,123,124}

These observations are generally attributed to the continuous buildup of fission gases, and their higher thermal diffusion than in the rest of the pellet. However, examinations using electron backscatter diffraction EBSD/SEM and focused ion beam FIB/SEM 3D examinations, have shown that grains in the center of high burnup fuel restructure into sub-micrometer sub-domains, with local crystal orientations near, but not identical to, those of the original grains (Fig. 37(a)). The intragranular fission gas bubbles previously considered as almost spherical are actually located on the boundaries between these sub-domains, and their shapes are similar to intergranular bubbles. The largest bubble shapes can be quite complex, the bubbles being surrounded by more than two sub-domains (Fig. 37(b)).^{81,125,126} No interconnection between these inter-sub-domain bubbles was found, nor any major intergranular bubble interconnection. This restructuring phenomenon should draw attention and calls for further detailed post-irradiation studies worldwide. It almost certainly plays a role for the enhanced fission gas release rates at high burnup, and more

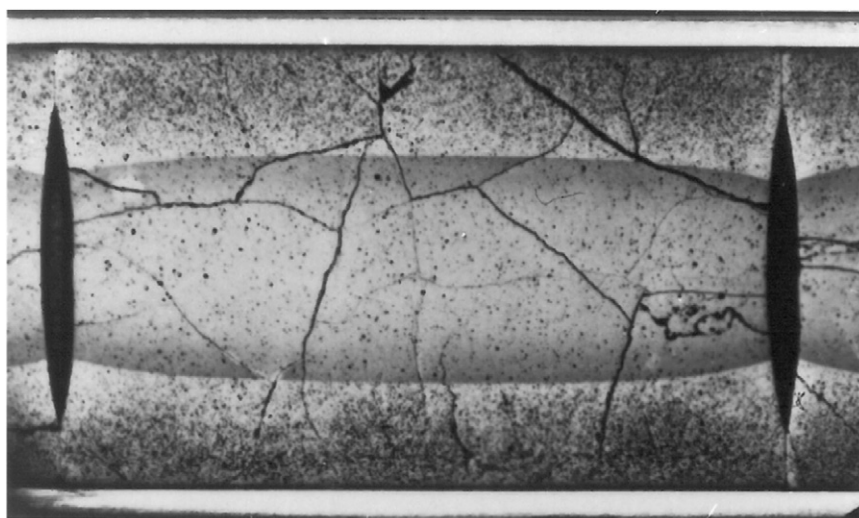


Fig. 36 Optical macrograph of a longitudinal cut of a 50 MWd kgM⁻¹ PWR fuel, after chemical etching, revealing small bubbles and grain boundaries. The very dark periphery corresponds to HBS. Around mid-radius there is a high density of sub-micron-sized bubbles, and in the center the bubble density is lower but their size larger. Reproduced from Guedeney, P., Trotabas, M., Boschiero, M., Forat, C., 1991. Standard PWR fuel rod characterization at high burn-up. In: Proceedings of the International Topical Meeting on LWR Fuel Performance. Avignon, France.

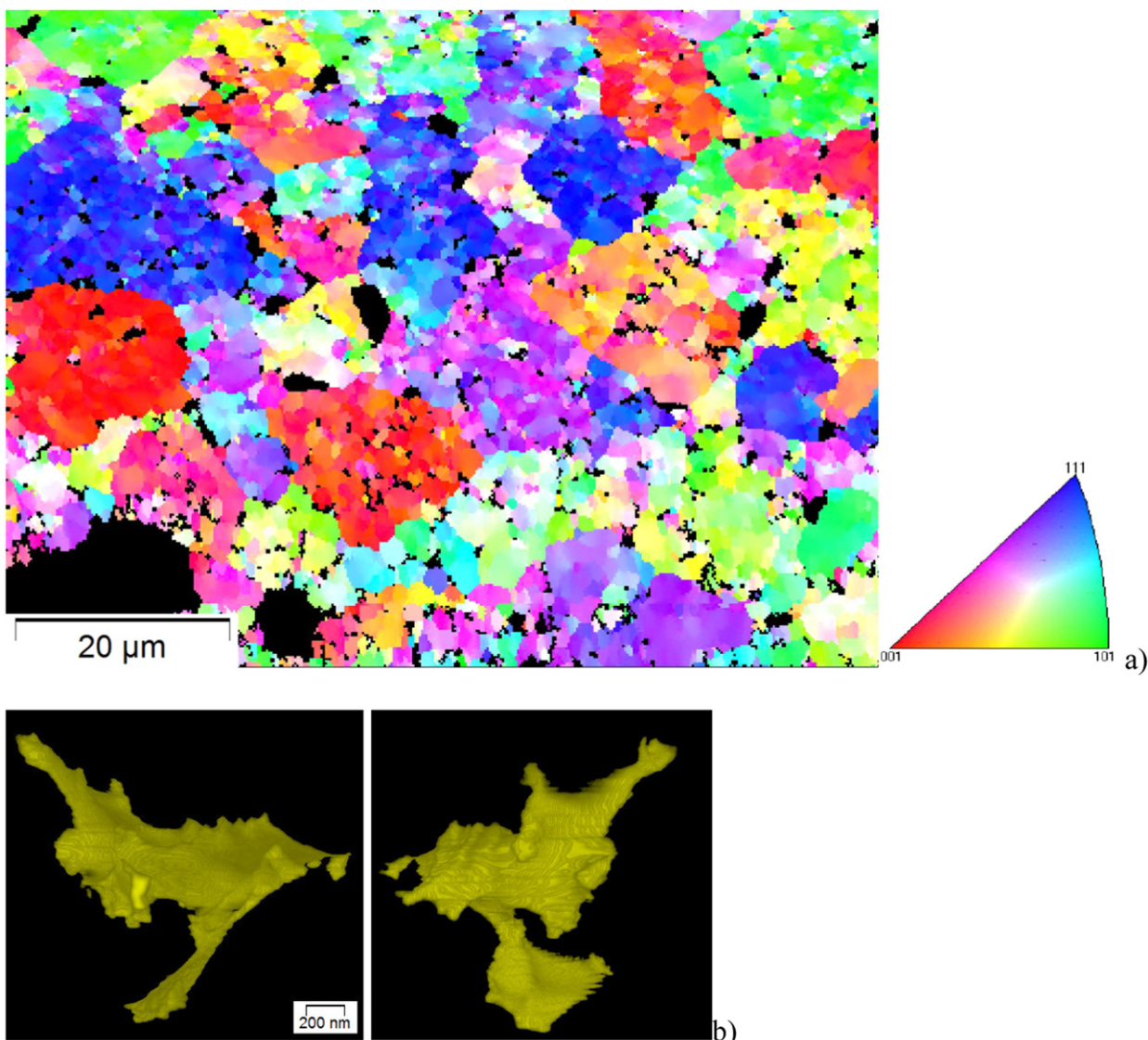


Fig. 37 73 MWd kgM⁻¹ PWR UO₂ center, (a) EBSD inverse pole figure map of the polished surface. The colors, give the local orientation of the crystal. Pure red, green, and blue colors are assigned to grains with respective <001>, <101> and <111> axes normal to the surface of the polished sample, (b) 2 views of the 3D reconstruction of an intragranular bubbles, inter-sub-domains. Reproduced from Noirot, J., Zacharie-Aubrun, I., Blay, T., 2018. Nucl. Eng. Technol. 50, 259–267.

observations and detailed examinations would be valuable input to the debates on the possible role of dislocations and grain boundaries for gas diffusion and release.^{127–129} Moreover, in LOCA situations, fuel fragmentation or cracking have also been observed in the central area of very high burnup fuel.^{97,98}

2.02.5 Transient Conditions

There are two families of transients to be considered:

- Normal transients, related, for example, to the controlled load follow operation in a PWR, with a maximum core power increase rate of 3% min⁻¹ (0.5 kW m⁻¹ min⁻¹), or control rod shuffling in a BWR, leading to high local power increase rates. The local power along a fuel rod can vary within a wider range than the mean core power, mainly due to the effect of control rods (in particular in a BWR), and the xenon-driven delayed neutron absorption (¹³⁵Xe) inherent to control rod/blade withdrawal.
- Transients with the potential for fuel rods to sustain a linear power increase rate of 10 kW m⁻¹ min⁻¹ (class 2) or even higher, up to around 100 kW m⁻¹ min⁻¹ in case of a reactivity insertion accident (RIA, class 4). When an abnormal core transient is detected by the core protection system, all control rods/blades are automatically inserted. In an accident scenario, immediately

before such a scram, fuel rods can be subject to a rapid and short local transient with a maximum power depending upon their remaining reactivity (e.g., $40\text{--}50 \text{ kW m}^{-1}$). For class 2 events, fuel rod design and operating rules have been established, to avoid any cladding failure. The reactor can then be restarted as soon as the origin of the transient is identified and remedied. The class 4 RIA accident is quite different, in that a single control rod assembly/blade is assumed to suddenly be ejected/dropped out of the core, no longer controlling local reactivity.

During a fast power increase, the main mechanical loading of the cladding is related to the differential thermal expansion between fuel and cladding. Fuel and cladding materials have similar thermal expansion coefficients, but their temperatures are very different. The cladding remains within the range of $350\text{--}400^\circ\text{C}$, while a range of $850\text{--}1250^\circ\text{C}$ is applicable for the fuel stack average temperature. The temperature gradient in the fuel ranges from 175 to $375^\circ\text{C mm}^{-1}$. This has several consequences:

- The hour-glassing phenomenon is amplified.
- The radial cracks in the fuel pellets open in the hoop (circumferential) direction, inducing a hoop shear stress on the cladding inner surface.
- The central part of the pellet passes from a purely elastic state to a viscoplastic behavior. In some cases, fuel material is able to flow in the axial direction, partly or totally filling the dishing.
- Fission gases and volatile elements are able to move quickly, and precipitate in intergranular and intragranular bubbles, trapping vacancies and leading to a gas swelling that adds to the total compressive stress, which may lead to resintering and grain growth in the central parts of the fuel.

The PCI/PCMI processes, well analyzed in the GONCOR analytical experiment performed in the SILOE reactor,¹³⁰ is the following:

- (1) During a power rise, the thermal expansion of the pellet induces stress and strain in the cladding. The level of the final hoop stress in the cladding depends upon the status (size) of the pellet-cladding gap previous to the ramp. When contact is already established prior to the ramp (conditioned situation), maximum stress is achieved. Due to the pellet hour-glassing, the initial stress is higher at the pellet-to-pellet interface than at mid-pellet. At this stage, several possibilities are to be considered: gap closure is achieved only locally at pellet ends, gap closure is total, or an intermediate situation prevails, involving friction. An initial ovality of the cladding and the presence of a radial pellet crack both favor stress localization/concentration on the cladding inner surface.
- (2) The end of the ramp is the critical period for inducing a potential cladding failure. Some volatile and corrosive species such as iodine, cadmium, or bromine, released by the fuel pellets during the ramp, can reduce the resistance of the clad material to stress-corrosion cracking (SCC), and help induce incipient cracks (1) in Fig. 38. If the local stress is high enough, the incipient crack can propagate (2) with a rate proportional to the power 9 of the stress intensity factor K_{ISCC} of the material. Initially, propagation is also facilitated by the presence of corrosive species, for example, iodine, but if/when the effective stress (σ_{real}) becomes higher than the ultimate stress of the cladding, a ductile shear drives crack propagation throughout the cladding wall (3). Often the first, SCC-driven part of the propagation is mainly intergranular.
- (3) The increase of the hoop stress in the cladding wall induces creep-out of the tubing, which gradually relaxes the stress. The stress relaxation is amplified by fuel creep in the central, hot, and viscous part of the pellets. At the same time, fission gases precipitate in bubbles in the hottest part of the pellet $>1100^\circ\text{C}$, inducing additional swelling of the material. As the gas swelling proceeds, it increases the hydrostatic stress in the fuel material, enhancing the plastic deformation toward the dishes. It may also lead to some resintering of the hottest part of the pellet. Nevertheless, fuel swelling leads to an increase of the pellet diameter. The GONCOR experiment¹³¹ has shown that the kinetics of all these processes is quicker at the pellet ends than at mid-pellet, presumably because the interaction stress is attained earlier and is higher at the pellet ends (effect of hour-glassing).
- (4) Finally, the swelling kinetics may lead (within 20 min in the GONCOR experiment) to the formation of secondary ridges at mid-pellet, which may be larger than the primary ridges, with heights ranging between 40 and 60 μm (in the GONCOR experiment).

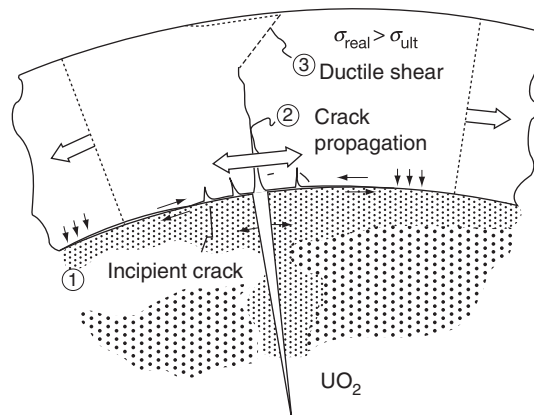


Fig. 38 Mechanisms leading to cladding failure.

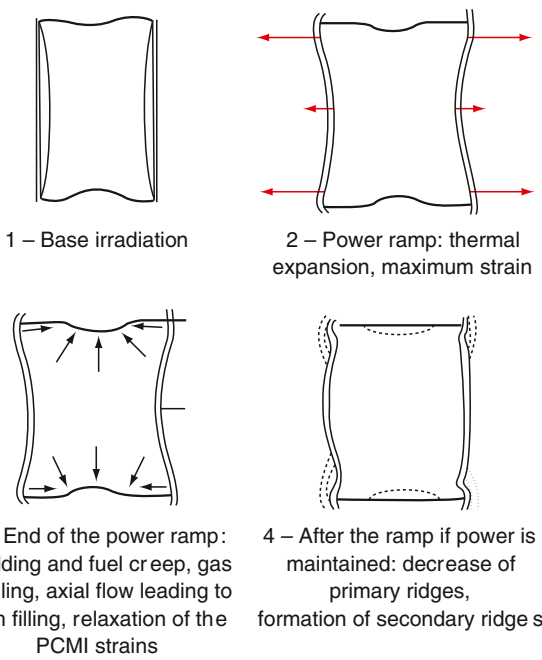


Fig. 39 Summary of the process induced by the power ramp.

Fig. 39 summarizes the process described above. The highest risk of PCI failure occurs within a few minutes after the ramp initiation and the failure is most likely to happen at the pellet-to-pellet interface (second drawing). There is no observed relationship to the final height of the secondary ridges (fourth drawing). The code simulations account also for fragment relocation.^{131–133}

The RIA accident is a quasi-adiabatic process with a very high ramp rate and short duration (1 min maximum). No diffusion processes or creep strains are involved due to the short duration. Cladding failure can be achieved by a quasi-uniform strain applied by the fuel on the cladding, exceeding the ultimate strain capability. The sudden change in dimension of the fuel pellets is due to the rapid thermal expansion, a reversed radial power generation, and the induction of grain separation. During a RIA pulse, the UO₂ displays a non-linear elasto-viscoplastic behavior, and, near the outer edges of the fuel, being under very high biaxial compression (~ 900 MPa for the highest energy pulses – area with high temperature/radial temperature gradient), the ductile deformation causes grain boundary decohesion.^{134,135} This grain boundary decohesion area is even more pronounced in a radial direction when the pulse width is reduced and significant energy is still deposited. Decohesion can also be caused by enhanced pressure in the inter-granular bubbles. The main question is not how the pellets are straining the cladding tube, but whether the cladding material is able to sustain this near-instantaneous strain. Indeed, grain boundary decohesion may lead to excessive localized fuel fragmentation, with small-dimension fragments, in its turn leading to extensive inter-granular fission gas release (gas created during irradiation under normal operating conditions and present in grain boundaries, dissolved or in the form of bubbles) into free volumes within the rod. This fission gas release can, in turn, lead to a pressure increase inside the fuel rod, and, therefore, additional stress on the cladding. Furthermore, such an enhanced gas release may compound any ballooning phenomena, should rod departure from nucleate boiling (DNB) occur. In addition, in the event of cladding failure during the RIA pulse (possible failure modes: failure through mechanical pellet-cladding interaction or through ballooning/bursting), the small-dimension fragments could be ejected and pulverized outside the cladding. From an industrial perspective, it is therefore crucial to study (through experiments and computer modeling) the behavior of fuel and fuel rods during an RIA pulse, with a view of assessing, in a cladding failure scenario, the fraction of fission gas that may be released to the reactor system, the volume fraction of fuel that could be ejected, and the size distribution of the corresponding fragments. All these estimates are also valid for MIMAS MOX fuels. However, during a RIA pulse, the heterogeneity of plutonium for MOX fuel means that local fission density will be different for each of the fuel phases, as will the temperature and the thermal expansion, the elasto-viscoplastic behavior and related damage (decohesion of grain boundaries).^{17,18,136} The RIA international projects have shown that the fuel enthalpy leading to clad failure is decreasing with the irradiation level of the material. Looking closer, it was demonstrated that the cladding outer oxide thickness was the crucial parameter, probably because it is associated with hydrogen pickup. Hydrogen can reduce the strength and ductility of Zr-based cladding, in particular when the hydrides are oriented in the radial direction. Also, at high burnup, when the zirconia layer reaches thicknesses around 100 µm, oxide spalling can lead to local cold spots in the cladding, inducing hydrogen migration and the formation of hydride blisters. These blisters constitute brittle points in the cladding. With modern, carefully optimized cladding materials, waterside oxide formation and the associated hydrogen pickup is highly reduced, compared to earlier variants, and so is the risk associated with cladding embrittlement by hydrogen.

2.02.6 Limiting Phenomena

Concerning limiting phenomena, some criteria have been established for the UO₂ and MOX fuel designs. Engineering must demonstrate that all relevant parameters fulfil those criteria at any time from the loading of the fuel to reprocessing, or during long-term storage. The key performance limiting phenomena are:

- (1) *Pellet-clad (mechanical) interaction (PCI/PCMI)*: Although this failure mode has limited consequences, certain limits may be imposed to prevent it. PCI/PCMI is a complex process with a maximum risk for failure when the fuel pellet to clad gap begins to close firmly and the reactivity of the fuel is still high, that is, in the 30–40 MWd kgM⁻¹ range. The risk is enhanced by pellet fragments inducing a local shear strain on the cladding, and by the chemical interaction kinetic at the interface, as outlined in Section 2.02.5. In order to prevent SCC, the cladding hoop stress calculated for normal operation and Class 2 transients is limited by certain vendors.

The control blade operation at power, typical for a BWR, creates a more severe PCI/PCMI challenge than in a PWR. Therefore, typical BWR fuel features a cladding liner, that is, a thin layer of a dilute, very ductile Zr alloy on the inside of the cladding. Such a liner creates a substantial additional margin to PCI failure.

Another consequence of PCMI is the hoop strain of the cladding caused by pellet swelling (see Section 2.02.3.3). Since this implies thinning of the cladding, which in turn reduces its strength, the extent of the total permanent hoop strain is limited during the whole lifetime of the fuel rods, typically to 1%.

In power plants that have to implement load follow, power cycling causes a repeated load to the cladding, which may lead to long-term fatigue and the ensuing crack initiation. The allowed (stress-dependent) number of cycles can be calculated and is limited by certain vendors.

- (2) *Cladding elongation and assembly bow*: During irradiation, the anisotropic character of the cladding material and the preferential migration of vacancies and interstitials in specific lattice planes drive an overall cladding axial growth, activated by the fast neutron flux. When hard contact is established between the pellet and the cladding, pellet axial elongation causes an additional axial cladding strain. All this can lead to fuel rod bow with pitch reduction between the rods, thus reducing thermal margins. Differential elongation of guide tubes in a PWR assembly can lead to an overall assembly bow, potentially problematic for control rod insertion, assembly reloading, and affecting local power in fuel rods at the assembly periphery. For BWR fuel, the same mechanisms can cause fuel channel deformation, 'channel bow,' leading to local thermal margin reduction, interference with control rod operation, as well as other issues. These phenomena are closely surveyed, and improvements in design and material have been, and are being, introduced to mitigate.
- (3) *Cladding oxidation and hydrogen pickup*: Concerning the ZrO₂ formation at the cladding waterside surface, a typical criterion is related to the ASTM criterion of a maximum cladding wall thickness reduction of 10%, which corresponds to an oxide thickness of the order of 100 µm. (The zirconia density is lower than the Zircaloy density: 6.6 g cm⁻³ compared to 7.7 g cm⁻³.) It is also important to avoid significant spalling of zirconia, which would induce local cold areas at the cladding surface leading to hydrogen accumulation by diffusion, and eventually degraded mechanical properties. The second aspect is the hydrogen pickup associated with corrosion of Zr in water. When the hydrogen concentration in the cladding exceeds the solubility limit, 70–100 ppm by weight at operating temperatures, zirconium hydrides will form. The impact of hydrides on key mechanical properties, i.e., strength and ductility, depends strongly on hydride distribution and orientation. Oxidation and hydrogen pickup are increasingly important at higher exposures, as the dependence on burnup is nonlinear.
- (4) *Cladding wear*: The criterion for cladding wear at the contact points between grid spring/dimples and the fuel rod is often also related to the ASTM criterion of a maximum cladding wall thickness reduction of 10%. Experience shows that considerably more wear is technically acceptable, that is, it will not cause failure due to local weakening of the cladding wall.
- (5) *Power to melt*: In LWR reactors, the use of uranium dioxide or MOX provides a comfortable power to melt margin. The uranium dioxide melting temperature is 2850°C for UO₂ and quite similar for MOX fuels. This temperature decreases slowly with burnup due to the dilution with fission products. It however remains above 2750°C. To achieve such temperatures, the linear heat rate must reach 700 W cm⁻¹, which is not realistic, even with the fuel initial reactivity. At high burnup, above 50 MWd kgM⁻¹, considering the fuel thermal conductivity decrease, the power to melt was estimated to be around 600 W cm⁻¹ (within the High Burnup Chemistry Project). Hence, the criterion is verified at any time of the irradiation.
- (6) *Fuel rod internal pressure*: Significant reopening of the radial gap between the fuel stack and the cladding must be avoided, to ensure at any time the heat transfer to the coolant. Otherwise, fuel overheating and excessive fission gas release can occur, ultimately leading to fuel failure. The original criterion required that the rod inner pressure must never exceed the outer coolant pressure. This criterion is over-conservative and has usually been replaced by a 'nonlift-off' criterion, that is, the radial creep-out of the cladding, driven by gas pressure in excess of the system pressure, must never exceed the expansion rate of the pellet associated with increasing burnup. Thus, the nonlift-off criterion ensures that the pellet-cladding gap does not open at high burnup. Experiments have shown that a large overpressure of the gas (considerably more than 5.0 MPa) is needed to initiate the reopening, i.e., lift-off.
- (7) *Departure from nucleate boiling ratio (DNBR)*: As described in Section 2.02.3.2, with increasing heat flux there comes a point at which the heat transfer from a fuel rod rapidly decreases due to the insulating effect of a steam blanket that forms on the rod surface, resulting in a severe increase of cladding temperature and possibly cladding failure. The ratio of the heat flux needed to cause departure from nucleate boiling (DNB) at given local coolant properties (pressure, enthalpy, mass flow rate) to the actual local heat flux of a fuel rod is defined as the DNBR. In class 1 and 2 conditions the DNBR of the most limiting rods has

to remain below the limit where DNB can be excluded with a 95% probability at a 95% confidence level. This phenomenon may limit the maximum allowed thermal power of a given PWR.

- (8) *Normal operation limits intended to ensure the fulfilment of accident criteria:* Constraints on the axial LHR distribution are typically applied at the core design level and during normal operation to guarantee that the conditions are never worse than those assumed in scenarios considered in the accident analyses. The maximum allowed LHR may depend on the axial position and on burnup, and can be reactor- and even cycle-specific. The fulfilment of the constraint is verified during the reload safety evaluation process as well as during plant operation.

2.02.7 Conclusions

The performance of uranium dioxide and MOX fuels in LWR nuclear reactors is well established. These fuels have demonstrated a very good behavior during irradiation, favored by their high melting temperature, providing large operating temperature margins. Some progress is still needed in the characterization of the mechanical properties of irradiated fuel. Experimentally, this is a tricky problem to solve, accounting for the drastic fuel pellet fragmentation in some accident scenarios, and the steep radial gradient in the nuclear fuel properties evolution. Nano-indentation, micro-indentation, micro-cantilever testing, acoustic techniques and creep tests under flux (techniques and systems used to measure mechanical properties on irradiated fuel and assess the related creep laws) are today potentially available in different laboratories (JRC,^{71,72} CEA⁷³) or test reactors (NRG Petten⁷⁴).

Due to the mild operating conditions compared to FBR reactors, the uranium dioxide matrix retains most of the fission products, even at very high burnup. The local fuel power variability is higher in BWR than in PWR, due to an axial gradient in the neutron spectrum and control blade operation. For these reasons, BWR fuel has evolved with the use of a PCI liner barrier. The addition of minor quantities of softening elements to the fuel pellet (chromium, niobium, aluminosilicates) is expected to increase PCI margins in both BWR and PWR fuel. Moreover, these additives favor manufacturing of large grain fuels, in order to delay the release of corrosive volatile fission products during power transient. The additives can also play a different role, modifying the oxygen potential, thus also modifying the fission product compounds formed in the hot central part during power transients. If chosen carefully, they might reduce the volume of gaseous species, and lead to less corrosive species.^{137,138}

The new and improved zirconium alloys first introduced in the 1980s enable higher discharge burnups, due to a reduction of cladding oxidation and hydrogen pickup, compared to the Zircalloys.

As the use of uranium dioxide is universal, international projects such as NFIR, SCIP, HBEP, HBRP, and HRP, etc., have provided the modelers with useful basic data or brought good insights about the relevant mechanisms. With the incredible progress in computer capability, and the large improvements in the knowledge base regarding the mechanisms active in fuel during irradiation, efficient tools are now available for fuel design. Modeling is still in progress, shifting gradually to multiscale approaches, or fundamental atomistic calculations, to assess parameters not attainable, up to now, by experimental characterization.

See also: 1.16 Ab Initio Electronic Structure Calculations for Nuclear Materials. 1.17 Interatomic Potential Development. 1.20 Primary Radiation Damage Formation in Solids. 1.21 Atomic-Level Dislocation Dynamics in Irradiated Metals. 1.23 Reaction Rate Theory. 1.24 Kinetic Monte Carlo Simulations of Irradiation Effects. 1.25 Phase Field Methods. 1.26 Computational Thermodynamics: Application to Nuclear Materials. 2.01 Uranium Oxide and MOX Production. 2.04 Burnable Poison-Doped Fuel. 2.05 Radiation Effects in UO₂. 2.06 Thermal Properties of Irradiated UO₂ and MOX. 2.07 Fission Product Chemistry in Oxide Fuels. 2.14 Modeling of Pellet Cladding Interaction. 4.03 Corrosion of Zirconium Alloys. 4.04 Corrosion and Stress Corrosion Cracking of Ni-Base Alloys. 6.09 Ceramic Coatings for Fusion Reactors

References

- Odelli, O., Edsinger, K., 2001. Optimum Cycle Length and Discharge Burnup for Nuclear Fuel – Comprehensive Study for BWRs and PWRs, Phase 1: Results Achievable Within the 5% Enrichment Limit. EPRI Technical Report 1003133.
- Gauld, I.C., Parks, C.V., 2000. Review of Technical Issues Related to Predicting Isotopic Compositions and Source Terms For High-Burnup LWR Fuel (NUREG/CR-6701). ORNL/TM-2000/277.
- Olander, D.R., 1976. Fundamental aspects of nuclear reactor fuel elements. In TID-26711-P1 – Technical Information Center – Energy Research and Development Administration. Berkeley: University of California.
- Bailly, H., Menessier, D., Prunier, C., 1999. The Nuclear Fuel of Pressurized Water Reactors and Fast Reactors. Paris: Lavoisier.
- Reynolds, A.B., 1996. Bluebells and Nuclear Energy. Madison, WI: Cogito Books.
- The Studsvik OVERRAMP Project. EPRI Report NP-3007, 1983. Research Project 1026-1.
- Djurle, S., 1984. Final Report of the SUPERRAMP Project. STSR-33. Studsvik.
- Lavake, J.C., Gaertner, M., 1984. High Burn Up PWR Ramp Test Program (DOE). Final Report DOE/ET/ 34030-10.
- Barner, J.O., Cunningham, M.E., Freshley, M.D., Lanning, D.D., 1985. High Burnup Effects Program – Summary Task 2. HBEP-45. Battelle Pacific Northwest Laboratories.
- Barner, J.O., Cunningham, M.E., Freshley, M.D., Lanning, D.D., 1990. High Burnup Effects Program – Final report. HBEP-61. Battelle Pacific Northwest Laboratories.
- Kinoshita, M., Kameyama, T., Kitajima, S., Matzke, H.J., 1998. J. Nucl. Mater. 252, 71–78.
- Sonoda, T., Matzke, H.J., Kinoshita, M., 1999. High burnup rim project. (IV) Threshold burn up of rim structure formation. In: Proceedings of the EHPG Meeting. Loen, Norway.
- Kinoshita, M., Matsumura, T., Kameyama, T., et al., 1994. High burnup rim project, irradiation program to study rim structure formation – Outline and preliminary analysis. In: Proceedings of the EHPG Meeting, 10/31–11/4. Bolkesjø.
- Kinoshita, M., 2001. HBRP – Final Report.

15. Kinoshita, M., Kameyama, T., 2005. HBRP_NT – Final Report No. 2.
16. Kinoshita, M., Yasunaga, K., Sonoda, T., *et al.*, 2008. Recovery and restructuring induced by fission energy ions in high burnup nuclear fuel. In: Proceedings of the SHIM. Lyon, France.
17. Papin, J., Lemoine, F., Federici, E., 2003. Main outcomes from the cabri tests results. In: Proceedings of the Topical Meeting on Ria Fuel Safety Criteria. Aix-en-Provence, France.
18. Papin, J., Cazalis, B., Frizonnet, J.M., *et al.*, 2007. Summary and interpretation of the CABRI REP-Na program, Nuclear Technology. 157, 23.
19. Blanpain, P., Arslan, M., Porsch, D., *et al.*, 2008. AREVA advanced MOX fuel assembly design and manufacturing. In: Proceedings of the Water Reactor Fuel Performance Meeting—WRFPM. Seoul, South Korea.
20. Blanpain, P., Thibault, X., Pages, J.-P., 1997. Proceedings of the International Topical Meeting on LWR Fuel Performance, pp. 39–45. Portland, USA.
21. Guérin, Y., Noirot, J., Lespiaux, D., *et al.*, 2000. Proceedings of the ANS International Topical Meeting on LWR Fuel Performance. Park City, UT, USA.
22. Federici, E., Courcelle, A., Blanpain, P., Cognon, H., 2007. Helium Production and Behavior in Nuclear Oxide Fuels During Irradiation in LWR. In Proceedings: International LWR Fuel Performance Meeting, 664–673. San Francisco (CA, USA), IAEA.
23. Pieragnoli, A., 2007. Influence of Sintering Additive Cr₂O₃ on Homogenization of Plutonium Distribution in a Heterogeneous MOX Pellet. University of Limoges.
24. Thomas, R., 2014. Chromium-Doped MOX: Optimization of Doping and Sintering Atmosphere. France: University of Bordeaux.
25. Delafoy, C., Jonnet, J., Rugama, Y., Garat, V., 2019. Plutonium recycling through LWR MOX fuel today and tomorrow. In: Proceedings of the International Conference on the Management of Spent Fuel From Nuclear Power Reactors: Learning From the Past, Enabling the Future. Vienna.
26. Soullard, J., 1976. Contribution à l'étude des défauts de structure dans le bixbyde d'Uranium. Ph.D. Work. Faculté des Sciences de Poitiers.
27. Spino, J., Papaioannou, D., 2000. J. Nucl. Mater. 281, 146–162.
28. Nogita, K., Une, K., 1994. Nucl. Instrum. Methods Phys. Res. Sect. B: Beam Interact. Mater. Atoms 91, 301–306.
29. Lassmann, K., Walker, C.T., van de Laar, J., 1998. J. Nucl. Mater. 255, 222–233.
30. Nukiyama, S., 1934. J. Japan Soc. Mech. Eng. 37, 367–374.
31. Marshall, T., Youchison, D.L., Cadwallader, L., 2001. Fusion Technol. 39.
32. Kreith, F., Manglik, R., Bohn, M.S., 2018. Principles of Heat Transfer, eighth ed. Cengage Learning.
33. Mac Adams, W.H., 1954. Heat Transmission. New York: McGraw-Hill.
34. MacDonald, P.E., Weisman, J., 1976. Nucl. Technol. 31, 357–366.
35. Berton, J.-P., Baron, D., Coquerelle, M., 1996. Chemical stability and physical properties of caesium uranates. In: Proceedings Technical Meeting of the Advances in Fuel Pellet Technology for Improved Performance at High Burnup. Tokyo: IAEA.
36. Baron, D., Couty, J.C., 1997. A Simulation of the Temperature Overshoot Observed at High Burnup in Annular Fuel Pellets. IAEA-TECDOC-957. International Atomic Energy Agency. pp. 303–312. (ISSN 1011-4289).
37. Lucuta, P.G., Matzke, H.J., Hastings, I.J., 1996. J. Nucl. Mater. 232, 166–180.
38. Baron, D., 1998. About the modelling of fuel thermal conductivity degradation at high burn-up accounting for recovering processes with temperature. In Seminar on Thermal Performance of High Burn-Up LWR Fuel. Cadarache: OECD-NEA.
39. Gomme, R.A., Yagnik, S., 1998. Understanding of Thermal Diffusivity Recovery with Thermal Annealing. EPRI TR 111068.
40. Gomme, R.A., Yagnik, S., 2000. Specific Heat Measurements and Post-test Characterization of Irradiated and Unirradiated Urania and Gadolinia Doped Fuel. EPRI Report TR 1000946.
41. Oguma, M., 1983. Nucl. Eng. Des. 76, 35–45.
42. Callu, C., Baron, D., Ruck, J.M., 1997. EDF fragment relocation model based on the displacement of rigid bodies. In: Proceedings of the International Conference on CANDU Fuel. Toronto, Canada.
43. Caillot, L., Delette, G., Julien, B., Couty, J.C., 1997. Impact of fuel pellet fragmentation on pellet-cladding interaction in a PWR fuel rods: results of the RECOR experimental programme. In: Proceedings of the Structural Mechanics in Reactor Technology (SMiRT). Lyon, France.
44. Ainscough, J.B., Oldfield, B.W., Ware, J.O., 1973. J. Nucl. Mater. 49, 117–128.
45. Kleykamp, H., 1985. J. Nucl. Mater. 131, 221–246.
46. Spino, J., Peerani, P., 2008. J. Nucl. Mater. 375, 8–25.
47. Cadarache, 2000. Fission gas behaviour in Water reactor fuels. In: Proceedings of the NEA/OCDE seminar, NEA, Ed., France: Cadarache.
48. Tonks, M., Andersson, D., Devanathan, R., *et al.*, 2018. J. Nucl. Mater. 504, 300–317.
49. Rest, J., Cooper, M.W.D., Spino, J., *et al.*, 2019. J. Nuclear Mater. 513, 310–345.
50. Setyawan, W., Cooper, M.W.D., Roche, K.J., *et al.*, 2018. J. Appl. Phys. 124, 075107.
51. Lewis, B.J., 1987. J. Nucl. Mater. 148, 28–42.
52. Walker, C.T., Knappik, P., Mogensen, M., 1988. J. Nucl. Mater. 160, 10–23.
53. White, R.J., 2000. The development of grain face porosity in irradiated oxide fuel. In Fission Gas Behaviour in Water Reactor Fuels. Cadarache: NEA/OECD, p. 189. (NEA ed.).
54. White, R.J., 2004. J. Nucl. Mater. 325, 61–77.
55. Noirot, J., Gonnier, C., Desgranges, L., *et al.*, 2009. LWR Fuel Gas Characterization at CEA Cadarache LECA-STAR Hot Laboratory. IAEA-TECDOC-CD-1635.
56. Turnbull, J.A., Friskney, C.A., Findlay, J.R., *et al.*, 1982. J. Nucl. Mater. 107, 168–184.
57. Rest, J., Hofman, G.L., 1991. Kinetics of recrystallization and fission-gas induced swelling in high burn-up UO₂ and U₃Si₂ nuclear fuels. In: Donelly, S.E., Evans, J.H. (Eds.), Fundamental Aspects of Inert Gases in Solids. New York: Plenum Press, p. 443.
58. Harding, J.H., Martin, D.G., 1989. J. Nucl. Mater. 166, 223–226.
59. Booth, A.H., 1957. A Method of Calculating Fission Gas Diffusion From UO₂ fuel and its Application to the X-2-f Loop Test. CRDC-721. Atomic Energy of Canada Limited.
60. Booth, A.H., Rymer, G.T., 1958. Determination of the Diffusion Constant of Fission Xenon in UO₂ Crystals and Sintered Compacts. 692. AECL.
61. Noirot, L., 2006. J. Nucl. Sci. Technol. 43, 1149–1160.
62. Noirot, L., 2011. Nucl. Eng. Des. 241, 2099–2118.
63. Jomard, F., Struzik, C., Bouloré, A., *et al.*, 2014. CARACAS: An industrial model for description of fission gas behavior in LWR-UO₂ fuel. In: Proceedings of the Water Reactor Fuel Performance Meeting (WRFPM), Sendai, Japan.
64. Bouloré, A., Struzik, C., Masson, R., *et al.*, 2017. Approach to better assess fission gas behaviors, applicable to fuels with complex microstructures. In: Proceedings of the Water Reactor Fuel Performance Meeting (WRFPM). Jeju Island, Korea.
65. Vitanza, C., Kolstad, E., Graziani, U., 1979. Fission gas release from UO₂ pellet fuel at high burn-up. In: Proceedings of the ANS Topical Meeting on Light Water Reactor Fuel Performance. Portland, OR.
66. Baron, D., Kinoshita, M., Thevenin, P., Largentton, R., 2009. Nucl. Eng. Technol. 41, 199–214.
67. Hiernaut, J.P., Wiss, T., Colle, J.Y., *et al.*, 2008. J. Nucl. Mater. 377, 313–324.
68. Matzke, H.J., 1994. J. Nucl. Mater. 208, 18–26.
69. Matzke, H.J., 1995. J. Nucl. Mater. 223, 1–5.
70. Noirot, J., Desgranges, L., Lamontagne, J., 2008. J. Nucl. Mater. 372, 318–339.
71. Spino, J., Cobos-Sabate, J., Rousseau, F., 2003. J. Nucl. Mater. 322, 204–216.

72. Baron, D., Masson, R., Gatt, J.M., *et al.*, 2005. Evolution of the nuclear fuel mechanical properties with burn-up: An Extensive European Experimental Program. In: Proceedings of the Water Reactor Fuel Performance, October 2–6, 2005. Kyoto, Japan.
73. Henry, R., Blay, T., Douillard, T., *et al.*, 2019. *Mech. Mater.* 136, 103086.
74. Knol, S., Koning, A.J.D., Groot, S.D., *et al.*, 2017. Creep measurements on LWR fuel during irradiation. In: Proceedings of the Water Reactor Fuel Performance Meeting (WRFPM). Jeju Island, Korea.
75. Baron, D., 1986. Abnormal porosity buildup in the fuel periphery at high burnup. In: Proceedings of the 9th High Burnup Effect Program (HBEP) Review, June 9, 1986. Wengen, Switzerland.
76. Barney, W.K., Wemple, B.D., 1958. Metallography of Irradiated UO₂-Containing Fuel Elements. KAPL-1836 AEC Research and Development Report. Knolls Atomic Power Laboratory.
77. Bleiberg, M.L., Berman, R.M., Lustman, B., 1963. Effects of high burn-up on oxide ceramic fuels. In: Proceedings Symposium on Radiation Damage in Solids and Reactor Materials. International Atomic Energy Agency. pp. 319–428.
78. Spino, J., Baron, D., Coquerelle, M., Stalios, A.D., 1998. *J. Nucl. Mater.* 256, 189–196.
79. Lozano, N., Desgranges, L., Aymes, D., Niepce, J.C., 1998. *J. Nucl. Mater.* 257, 78–87.
80. Spino, J., Papaioannou, D., Ray, I.L.F., Baron, D., 2000. Rim formation and fission gas behaviour: Some structure remarks. In *Fission Gas Behaviour in Water Reactor Fuels*. Cadarache: OCDE, pp. 247–268. (NEA ed.).
81. Gerczak, T.J., Parish, C.M., Edmondson, P.D., *et al.*, 2018. Restructuring in high burnup UO₂ studied using modern electron microscopy. *J. Nucl. Mater.* 509, 245–259. ISSN 0022-3115, doi:10.1016/j.jnucmat.2018.05.077. (<https://www.sciencedirect.com/science/article/pii/S0022311517316240>).
82. Kinoshita, M., Yasunaga, K., Sonoda, T., *et al.*, 2009. *Nucl. Instrum. Methods Phys. Res. Sect. B: Beam Interact. Mater. Atoms* 267, 960–963.
83. Kinoshita, M., 1996. High burnup rim project, (II) progress of irradiation and preliminary analysis. In EHPG. Loen: OECD Halden Reactor Project.
84. Kinoshita, M., Kitajima, S., Kameyama, T., *et al.*, 1997. Burnup rim project, progress of irradiation and preliminary analysis. In: Proceedings of the ANS LWRFP, March 2–6, 1997, pp. 530–535. Portland, OR.
85. Kinoshita, M., Sonoda, T., Kitajima, S., *et al.*, 2000. Proceedings of the ANS LWRFP. Park City, UT. pp. 590–603.
86. European Commission, 2008. F-Bridge Project, Basic Research for Innovative Fuel Design for GEN IV Systems, Annexe1 – Description of the Work, Seventh Framework Programme Euratom. European Commission.
87. Nogita, K., Une, K., 1995. *J. Nucl. Mater.* 226, 302–310.
88. Spino, J., Stalios, A.D., Santa Cruz, H., Baron, D., 2006. *J. Nucl. Mater.* 354, 66–84.
89. Romano, A., Horvath, M.I., Restani, R., 2007. *J. Nucl. Mater.* 361, 62–68.
90. Noiroit, J., Desgranges, L., Marimbeau, P., 2000. Contribution of the rim to the overall fission gas release: what do isotopic analyses reveal. In *Fission Gas Behaviour in Water Reactor Fuels*. Cadarache: NEA/OECD, p. 223. (NEA ed.).
91. Desgranges, L., Valot, C., Pasquet, B., *et al.*, 2008. *Nucl. Instrum. Methods Phys. Res. Sect. B: Beam Interact. Mater. Atoms* 266, 147–154.
92. Noiroit, J., Zacharie-Aubrun, I., Desgranges, L., *et al.*, 2009. *Nucl. Eng. Technol.* 41, 155–162.
93. Noiroit, J., Pontillon, Y., Yagnik, S., *et al.*, 2013. Proceedings of the EHPG. Storefjell.
94. Maeda, K., Asaga, T., 2004. *J. Nucl. Mater.* 327, 1–10.
95. Maeda, K., Tanaka, K., Asaga, T., Furuya, H., 2005. *J. Nucl. Mater.* 344, 274–280.
96. Noiroit, J., Lamontagne, J., Nakae, N., *et al.*, 2013. *J. Nucl. Mater.* 442, 309–319.
97. Noiroit, J., Blay, T., Lamontagne, J., *et al.*, 2015. Size and radial origin of fragments formed while heating a 83 GWd/tU PWR fuel up to 1200°C. In: Proceedings of the LOCA Workshop, Fuel Fragmentation, Relocation and Dispersal (FFRD) – Experimental Basis, Mechanisms and Modelling Approaches. Aix-en-Provence, France.
98. Report on Fuel Fragmentation, Relocation, Dispersal. NEA/CSNI/R(2016)16, OECD/NEA.
99. Wiesenack, W., 2015. Summary of HRP IFA-650 LOCA experiments with respect to FFRD. In: Proceedings of the LOCA Workshop, Fuel Fragmentation, Relocation and Dispersal (FFRD) – Experimental Basis, Mechanisms and Modelling Approaches. Aix-en-Provence, France.
100. Puranen, A., Granfors, M., Askeljung, P., *et al.*, 2013. Proceedings of the TopFuel, 2013. Charlotte, USA.
101. Flanagan, M.E., Oberlander, B.C., Puranen, A., 2013. Proceedings of the TopFuel, 2013. Charlotte.
102. Flanagan, M.E., Askeljung, P., Puranen, A., 2013. Post-Test Examination Results from Integral, High-Burnup, Fueled LOCA Tests at Studsvik Nuclear Laboratory. NUREG-2160. United States Nuclear Regulatory Commission.
103. Askeljung, P., Flygare, J., Minghetti, D., 2012. NRC LOCA testing program at Studsvik, recent results on high burnup fuel. In: Proceedings of the TopFuel 2012. Manchester.
104. Raynaud, P.A.C., 2012. Fuel Fragmentation, Relocation, and Dispersal During the Loss-of-Coolant Accident (NUREG-2121). United States Nuclear Regulatory Commission.
105. Noiroit, J., Pontillon, Y., Yagnik, S., *et al.*, 2014. *J. Nucl. Mater.* 446, 163–171.
106. Colle, J.Y., Hiernaut, J.P., Wiss, T., *et al.*, 2013. *J. Nucl. Mater.* 442, 330–340.
107. Baron, D., Hermitte, B., Piron, J.P., 1996. An attempt to simulate the porosity build-up in the rim at high burn-up. In: Proceedings of the Technical Committee Meeting on Advances in Pellet Technology for Improved Performance at High Burn-Up. Tokyo, Japan.
108. Kinoshita, M., 1997. *J. Nucl. Mater.* 248, 185–190.
109. Likhanskii, V.V., Khoruzhii, O.V., Sorokin, O.V., 2004. Physical model of rim-layer formation in UO₂ fuels. In: Proceedings of the International Workshop on the High Burn-up Structure in Nuclear Fuels, June, 28–30. Karlsruhe, Germany.
110. Rest, J., 2004. *J. Nucl. Mater.* 326, 175–184.
111. Rest, J., 2005. *J. Nucl. Mater.* 346, 226–232.
112. Khvostov, G., Novikov, V., Medvedev, A.V., Bogatyr, S., 2005. Approaches to modeling of high burn-up structure and analysis of its effects on the behaviour of light water reactor fuels in the START-3 fuel performance code. In: Proceedings of the Water Reactor Fuel Performance JNS-ENS-ANS Meeting, October 2–6. Kyoto, Japan.
113. Pizzocri, D., Cappia, F., Luzzi, L., *et al.*, 2017. *J. Nucl. Mater.* 487, 23–29.
114. Tarasov, V.I., Polovnikov, P.V., Shestak, V.E., Veshchunov, M.S., 2019. *J. Nucl. Mater.* 517, 214–224.
115. Veshchunov, M.S., Tarasov, V.I., 2017. *J. Nucl. Mater.* 488, 191–195.
116. Xiao, H., Long, C., 2016. *Nucl. Eng. Technol.* 48, 1002–1008.
117. Xiao, H., Long, C., Chen, H., 2016. *J. Nucl. Mater.* 471, 74–79.
118. Van Uffelen, P., Hales, J., Li, W., *et al.*, 2019. *J. Nucl. Mater.* 516, 373–412.
119. Guedeney, P., Trotabas, M., Boschiere, M., Forat, C., 1991. Standard PWR fuel rod characterization at high burn-up. In: Proceedings of the International Topical Meeting on LWR Fuel Performance. Avignon, France.
120. Ronchi, C., Sheindlin, M., Staicu, D., Kinoshita, M., 2004. *J. Nucl. Mater.* 327, 58–76.
121. Kulacsy, K., 2015. *J. Nucl. Mater.* 466, 409–416.
122. Esnoul, C., Michel, J.-C., Michel, B., *et al.*, 2015. Use of a micromechanical approach to investigate transient fuel fragmentation mechanisms. In: Proceedings of the LOCA Workshop. Aix-en-Provence.
123. Noiroit, J., Noiroit, L., Desgranges, L., *et al.*, 2004. Proceedings of the ANS LWR Fuel Performance. Orlando, FL, USA.
124. Stehle, H., 1988. *J. Nucl. Mater.* 153, 3–15.
125. Noiroit, J., Zacharie-Aubrun, I., Blay, T., 2018. *Nucl. Eng. Technol.* 50, 259–267.

126. Jädernäs, D., Corleoni, F., Puranen, A., *et al.*, 2013. Microstructural and chemical characterization of ramp tested additive fuel. In: Proceedings of the TopFuel 2013, September 15–19, 2013. Charlotte, NC.
127. Shea, J.H., 2018. *J. Nucl. Mater.* 501, 302–311.
128. Shea, J.H., 2019. *J. Nucl. Mater.* 522, 246–254.
129. Murphy, S.T., Fossati, P., Grimes, R.W., 2015. *J. Nucl. Mater.* 466, 634–637.
130. Garcia, P., Struzik, C., Agard, M., Louche, V., 2002. *Nucl. Eng. Des.* 216, 183–201.
131. Garcia, P., Moyne, M., 1997. Modelling the steady state and transient mechanical behaviour of fuel rods. In: Proceedings of the 14th International Conference on Structural Mechanics in Reactor Technology (SMIRT 14). Lyon, France.
132. Helfer, T., Garcia, P., Ricaud, J.M., *et al.*, 2004. Modelling the effect of oxide fuel fracturing on the mechanical behaviour of fuel rods. In Pellet-clad Interaction in Water Reactor Fuels Seminar Proceedings. Aix-en-Provence: OECD, NEA, pp. 367–377.
133. Proceedings of the Pellet-Clad Interaction in Water Reactor Fuels Seminar, 2004. OECD, NEA, Aix-en-Provence.
134. Salvo, M., Sercombe, J., Helfer, T., *et al.*, 2015. *J. Nucl. Mater.* 460, 184–199.
135. Lespiaux, D., Noirot, J., Menut, P., 1997. Proceedings of the International Topical Meeting on LWR Fuel Performance. Portland, USA.
136. Lemoine, F., 2006. *J. Nucl. Sci. Technol.* 43, 1105–1113.
137. Pennisi, V., Matheron, P., Riglet-Martial, C., *et al.*, 2015. Study of Niobium in UO₂ advanced fuel doped with NbOx. In: Proceedings of the ANS Annual Meeting, Division 10, Materials Science and Technology, Session e, Nuclear Fuels. San Antonio, USA.
138. Riglet-Martial, C., Sercombe, J., Lamontagne, J., *et al.*, 2016. *J. Nucl. Mater.* 480, 32–39.
139. Ciszak, C., Desgranges, L., Garcia, P., *et al.*, 2019. *J. Nucl. Mater.* 520, 110–120.
140. Ciszak, C., Mermoux, M., Miro, S., *et al.*, 2017. *J. Nucl. Mater.* 495, 392–404.
141. Lassmann, K., Walker, C.T., van de Laar, J., Lindström, F., *et al.*, 1995. *J. Nucl. Mater.* 226, 1–8.